

UNIVERSITY OF OXFORD

MENG 4YP REPORT

**Gas Sensing for Cooling and Combustion using
Micro-Electro-Mechanical Systems:
A Proof of Concept Study**

Author:

Kazuki TOJO

Supervisors:

Professor Kam CHANA

Professor John COULL

Oxford Thermofluids Institute
Department of Engineering Science

May 16, 2023



UNIVERSITY OF OXFORD

Abstract

Oxford Thermofluids Institute, Department of Engineering Science

Gas Sensing for Cooling and Combustion using Micro-Electro-Mechanical Systems: A Proof of Concept Study

by Kazuki TOJO

Currently, there is a gap in the market for high frequency gas sensing. The fastest methods of gas sensing operate at 0.1 Hz, whereas for turbomachinery applications, we are interested in frequencies of up to 100 kHz or more.

A novel approach to gas sensing through heat transfer is introduced, utilising the principle of thermal products—a thermal property unique to every material, calculated by $\sqrt{\rho c_p k}$, where ρ is density, c_p is specific heat capacity and k is thermal conductivity. It is possible to identify the material, or the composition of a mixture of materials, by quantifying the thermal product at a sufficiently high signal-to-noise ratio. By pulsing a thin-film, which is essentially a resistor, with a step current, heat is generated and the heat transfer between the film and its surroundings can be measured. This heat transfer is dependent on the thermal product of the surroundings, which varies with gas concentration. Therefore, the response of the thin-film can be used to measure gas concentration.

The thin-film concept is developed into a microscale sensor package with the Flusso FLS110 MEMS gas flow sensor, which implements two tungsten resistors that can be operated as thin-films. Its miniature size allows for high frequency and sensitivity, although it also means that internal conduction and convection occurs rapidly. Therefore, the sensor was modelled through a finite-elements approach as a network model in MATLAB to capture the unique heat transfer of the specific sensor.

The Flusso sensor showed good sensitivity to air, argon and exhaled breath, revealing a 8.39 K (4.66 %) difference between final temperatures of ambient air and argon—around 100 times larger than the maximum uncertainty of 0.0539 %. The sensor also operated at 200 Hz, improving measurement frequency by three orders of magnitude compared to the fastest gas analysers currently on the market.

Impact Statement

Title: Gas Sensing for Cooling and Combustion using Micro-Electro-Mechanical Systems: A Proof of Concept Study

Team: Kazuki Tojo, Professor John Coull, Professor Kam Chana (University of Oxford)

Issue: The aviation industry is responsible for a significant fraction of global carbon emissions. To mitigate these emissions, we can increase jet engine thermal efficiency by raising the temperature of combustion, which is achieved through the use of coolant air to maintain the integrity of parts. Therefore, blade film cooling is a significant area of research to achieve higher efficiency in the industry. However, current gas analysers lack the sufficient measurement frequency for instantaneous and unsteady measurements. The fastest gas sensing techniques operate at 0.1 Hz, whilst measurement frequencies of up to 100 kHz would be useful.

What Has Been Done: Gas analysis technology is in continuous development. Amongst various gas sensing methods including infrared, electrochemical and gas chromatography techniques, calorimetric sensing performs fastest with response times of 10 s to 15 s.

Impact: We investigated a novel approach to gas sensing through heat transfer by measuring a fluid's heat transfer with a thin-film gauge using the principle of thermal products. We successfully tested this concept with the Proxisense handheld thin-film sensor and further developed it into a sensor package with the Flusso FLS110 MEMS gas flow sensor. This exploits the miniature size of the sensor ($1300 \times 1600 \mu\text{m}$) to achieve high sensitivity and measurement frequency. Ultimately, we managed to operate the sensor as a gas analyser with sufficient sensitivity and achieved a measuring frequency of 200 Hz, three orders of magnitude faster than current gas analysers.

We also identified ideas to further develop this technology into a sensor with even higher frequency that can be directly embedded into turbomachinery experiments. This will enable novel methods of conducting and analysing turbomachinery experiments, allowing for significant improvement in the development of an increasingly efficient aviation industry.

Contact: Kazuki Tojo, St. Hilda's College, Cowley Place, Oxford, OX4 1DY, England

Acknowledgements

I would like to express my sincere appreciation for the support and guidance of my two supervisors, Professor Kam Chana and Professor John Coull. Despite the jump from a different institution, their patience and understanding allowed for a challenging but smooth introduction to this project. Their expert knowledge, constructive criticism and insightful feedback were crucial to my growth as a learner and researcher this past year.

I would also like to thank Liam Boland and Jamie Dean for their technical expertise and assistance. From soldering the microscale MEMS sensors to setting up gas analysis experiments, their attention to detail and logistical flexibility were essential to the success of the practical aspect of this project, ensuring a high standard of quality and accuracy.

I am also very grateful for the helpful assistance of Manuela Sisti, particularly for thoroughly preparing me to conduct the water bath calibrations. Her enthusiasm and passion, as well as her willingness to help despite her busy schedule, was greatly appreciated.

Finally, my deepest gratitude goes out to my family and friends, both at Oxford and Princeton, for their continuous love and support throughout this academic journey. Their constant encouragement has been a strong source of motivation, particularly as I worked to the make the most of what has been a challenging but truly memorable exchange program.

Thank you all so much for being a part of this journey. It has been a truly memorable and rewarding experience.

Contents

Abstract	i
Impact Statement	ii
Acknowledgements	iii
List of Figures	vii
List of Symbols	x
1 Introduction	1
1.1 Motive	1
1.2 Principle of Measurement	1
1.2.1 Goal	2
2 Literature Review	3
2.1 Measuring Film Cooling Effectiveness	3
2.2 Current Techniques for Gas Analysis	3
2.2.1 Non-Dispersive Infrared Gas Sensing	4
2.2.2 Electrochemical Gas Sensing	4
2.2.3 Calorimetric Gas Sensing and Gas Chromatography	4
2.3 Thin-Film Gauges	5
2.3.1 Principle	5
2.3.2 Sensor Structure, Construction and Manufacturing	6
2.4 Thin-Film Gauge Heat Transfer Measurements	7
2.4.1 Measurements by Thermal Product	7
2.4.2 Application to Gas Sensing: MEMS Thin-Films	7
3 Research Question	9

4 Experimental Methods	10
4.1 Experimental Setup	10
4.2 Data Collection	11
4.3 Water Bath Calibration	12
4.3.1 Principle	13
4.3.2 Settings and Procedure	14
4.3.3 Results: Flusso MEMS Sensor	15
4.3.4 Results: Proxisense Thin-Film Gauge	15
5 Proxisense Thin-Film Gauge	17
5.1 1D Model	17
5.1.1 Derivation	17
5.1.2 Limitations	19
5.1.3 Alternative Options of Modelling	19
5.2 Experimental Procedure	20
5.3 1D Model Validation	21
5.4 1D Model Predictions	21
5.4.1 Air-CO ₂ Mixture	21
5.4.2 Enhancing Temperature Differences	23
5.4.3 Air-Argon Mixture	24
5.5 Improvements for Increased Sensitivity	24
6 Flusso MEMS Sensor	27
6.1 Network Model	28
6.1.1 Derivation	28
6.1.2 Limitations	30
6.2 Experimental Procedure	31
6.2.1 Soldering Connections	31
6.2.2 Settings and Procedures	32
6.3 Preliminary Investigations	33
6.4 Initial Tests	34
6.5 Preliminary Results: Ambient Air and Flowing Breath	36
6.5.1 Setup	36

6.5.2	Results	36
6.6	Preliminary Results: Flowing Air and Flowing Argon	37
6.6.1	Setup	37
6.6.2	Results	38
6.7	Undamaged Sensor Results: Ambient Air vs. Argon	38
6.7.1	Setup	38
6.7.2	Results	39
6.8	Network Model Validation	40
6.9	Tuned Network Model	40
7	Conclusions & Future Work	42
7.1	Conclusions	42
7.2	Future Work	43
Bibliography		45

List of Figures

1.1 Basic concept of turbine blade film cooling. Extracted from Figure 1 of Li et al. [1].	2
2.1 A thin-film gauge developed and manufactured by Proxisense, consisting of two thin-film circuits.	5
4.1 Identification of the starting point to omit starting processes.	11
4.2 User interface of Proxisense software.	11
4.3 Identification of the starting point to omit starting processes. In this experiment, the 11 th data point is taken as the starting point.	12
4.4 Final curve after omitting starting processes.	12
4.5 K-type thermocouple.	13
4.6 Proxisense sensor made water-tight with two layers of plastic sleeves.	13
4.7 Thermocouples secured onto each side of the Proxisense sensor's MACOR® substrate using Kapton® tape.	14
4.8 Water bath calibration of Flusso sensor. Errors bars represent the 0.75 % uncertainty of the K-type thermocouple.	16
4.9 Water bath calibration of Proxisense sensor. Errors bars represent the 0.75 % uncertainty of the K-type thermocouple.	16
5.1 Proxisense thin-film gauge, displayed again for reference.	17
5.2 1D semi-infinite model, visualised at the cross-section of a thin-film structure. Note that, in this specific case, q_s represents heat flux into the substrate.	19
5.3 Experimental setup of the Proxisense sensor in deionised water.	21
5.4 Temperature plotted against time from pulsing of Proxisense sensor with 300 mA step currents of length 167 ms, alongside comparison with 1D model prediction. Error bars for all plots in Section 5 were placed at one standard deviation from the data point.	22

5.5	Temperature plotted against square root of time from pulsing of Proxisense sensor with 300 mA step currents of length 167 ms, alongside comparison with 1D model prediction.	22
5.6	1D model prediction of a range of compositions of an air-CO ₂ mixture.	23
5.7	Integral of the air-CO ₂ heat curves in Figure 5.6.	24
5.8	1D model prediction of a range of compositions of an air-argon mixture.	25
5.9	Integral of the air-argon heat curves in Figure 5.8.	25
6.1	Basic structure of the Flusso sensor, along with its size scale. Extracted from Figure 1 of Gardner et al. [24].	27
6.2	Two flow configurations of the Flusso mass flow sensor. Extracted from Figure 2 of the FLS110 Miniature Gas Flow Sensor Datasheet [36].	27
6.3	Finite-elements network model, visualised at the cross-section orthogonal to the <i>x</i> -axis in Figure 6.1. The discretisation is kept low to <i>n</i> = 10 for clarity. In the actual MATLAB model, the sensor is discretised beyond <i>n</i> = 60.	29
6.4	Network model assumes infinite length of sensor and ignores lateral conduction.	31
6.5	Flusso MEMS sensor with soldered connections to a 9-pin D-sub connector.	32
6.6	Pin and port positions on the Flusso sensor. Extracted from Figure 8 of the FLS110 Miniature Gas Flow Sensor Datasheet [36].	32
6.7	Pulses with the Flusso sensor at 10 mA would initially completely plateau at 5 V.	34
6.8	Pulsing of the Flusso sensor at 10 mA for pulse lengths of 5 ms. Error bars for all plots in Section 6 were placed at one standard deviation from the data point.	35
6.9	Pulsing of the Flusso sensor at 15 mA for pulse lengths of 5 ms.	35
6.10	Result comparison of Flusso sensor pulsing experiments at 15 mA for pulse lengths of 5 ms in air and breath.	37
6.11	Result comparison of Flusso sensor pulsing experiments at 15 mA for pulse lengths of 5 ms in flowing air and argon.	38
6.12	Result comparison of Flusso sensor pulsing experiments at 15 mA for pulse lengths of 5 ms in ambient air and argon.	39
6.13	Original, untuned network model plotted with the initial constant heat flux setting against the updated constant current setting. The network model was executed in 5 μ s time increments with 120 discretisations along half the sensor length. Note that there are two pairs of separate model curves that are overlapping.	40

6.14 Flusso sensor pulsing experiments at 15 mA for pulse lengths of 5 ms in ambient air and argon, plotted against the tuned network model. The tuned network model was executed in 5 μ s time increments with 120 discretisations along half the sensor length.

List of Symbols

ρ	density	kg m^{-3}
c_p	specific heat capacity	$\text{J kg}^{-1} \text{K}^{-1}$
k	thermal conductivity	$\text{W m}^{-1} \text{K}^{-1}$
R	resistance	Ω
T	temperature	K or $^{\circ}\text{C}$ as specified
α	temperature coefficient of resistance	K^{-1}
P	power	W
I	current	A
V	voltage	V
x	distance	m
y	distance	m
t	time	s
q	heat flux density	W m^{-2}
Q	rate of heat transfer	W
h	convective heat transfer coefficient	$\text{W m}^{-2} \text{K}^{-1}$
m	mass	kg
w	width	m
n	unit	
L	length	m
Nu	Nusselt number	

MEMS	Micro-Electro-Mechanical Systems
SNR	Signal-to-Noise Ratio
PSP	Pressure-Sensitive Paint
CCD	Charge-Couple Device
TSP	Temperature-Sensitive Paint
IR	InfraRed
NDIR	Non-Dispersive InfraRed
TCR	Temperature Coefficient of Resistance
CAD	Computer-Aided Design
CFD	Computational Fluid Dynamics

1 Introduction

In turbomachinery, cooling remains one of the most important aspects to be considered. On a fundamental level, the second law of thermodynamics states that the efficiency of a heat engine increases with temperature—the maximisation of temperature is, therefore, desired and achieved through the use of coolant air to maintain the integrity of parts. As such, experimental testing of cooling technologies is critical in turbomachinery development, allowing for better understanding of cooling phenomena such as turbine blade film cooling (*Fig. 1.1*). With such applications, temperature ratios ($\frac{T_c}{T_g} \approx \frac{1}{2}$ in Figure 1.1) and density ratios are of particular importance.

1.1 Motive

During research and development, it is common to emulate the coolant-to-mainstream density ratios in a high-pressure turbine by exploiting the varying properties of different gases. In particular, CO₂ or argon are often used as a tracer gas, with recent studies also implementing SF₆ [2], allowing for the simultaneous use of dual gases. Such tracer gases must be experimentally tracked to obtain their concentrations for the purpose of understanding cooling effectiveness through the mass/heat transfer analogy. Currently, several gas sensing techniques are widely applied in engineering, including optical methods, semiconductor sensing, calorimetric methods and gas chromatography [3]. However, there still persist major drawbacks, particularly in the form of long response times and high costs. For example, a CO₂ analyser on the current market takes ≈ 20 s for CO₂ sensing by infrared and ≈ 60 s for O₂ sensing by electrochemical cell [4]. Another SF₆ analyser quotes a response time of ≈ 9 min for sensing by electrochemical reaction [5].

1.2 Principle of Measurement

We introduce heat transfer as a novel approach to gas sensing. Every material, and thereby any mixture of materials, carries a unique thermal property—this is the principle of the measurement. In fluids, this thermal property can be expressed by $\sqrt{\rho c_p k}$, hereinafter referred to as the "thermal

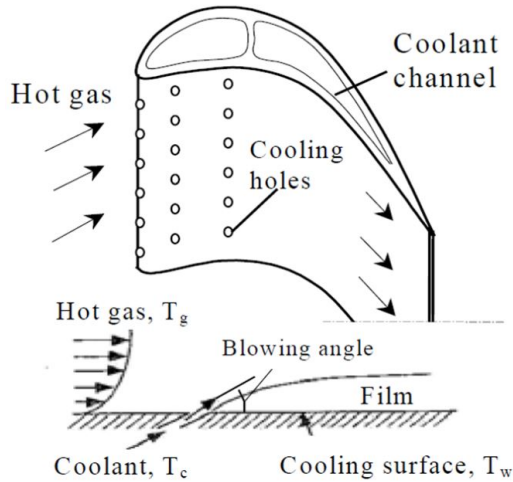


FIGURE 1.1: Basic concept of turbine blade film cooling. Extracted from Figure 1 of Li et al. [1].

product", where ρ is density, c_p is specific heat capacity and k is thermal conductivity. By quantifying this at a sufficiently high signal-to-noise ratio (SNR), it is possible to identify a single material, or the composition of a mixture of materials.

Whilst slow methods of gas sensing can obtain averages, there is a need in turbomachinery for measurements of instantaneous or unsteady states. As an example, a 60-blade turbine operating at 9500 rpm would have a 9500 Hz blade pass frequency, thereby requiring a measurement frequency of 95 kHz to obtain at least 10 data points at each blade pass frequency. Fundamental experiments may need lower frequency. Through gas sensing by heat transfer, we seek whether it is possible to develop a high frequency gas analysis system for such applications. The thermal products, $\sqrt{\rho c_p k}$, of air, CO₂ and argon are 5.6295, 5.0380 and 3.8676 respectively [6]—relative to air, CO₂ has a 10.5 % smaller thermal product and argon has a 31.3 % smaller thermal product. We attempt to exploit these differences by measuring the heat transfer properties of gases using thin-film gauges.

1.2.1 Goal

Ultimately, we aim to develop the thermal product approach into a microscale sensor package through micro-electro-mechanical systems (MEMS) technology. Such a sensor would have a length scale of under 2 mm, allowing it to be directly embedded in experiments for gas analysis. MEMS sensors also enable high measurement frequency and sensitivity, as well as low-cost and large-scale manufacturing.

2 Literature Review

This literature review will begin by exploring techniques to measure film cooling effectiveness, followed by a more thorough investigation of current gas sensing methods and their suitability to analyse tracer gases in film cooling. The concept of thin-film gauges will then be introduced, along with current applications and manufacturing methods. Finally, a novel use of thin-film gauges is discussed as a potential solution to achieve high frequency gas analysis.

2.1 Measuring Film Cooling Effectiveness

There are various methods used in industry to measure turbine blade film cooling. Pressure-sensitive paint (PSP) is widely used as a non-intrusive method of visualising film cooling, as it is a photoluminescent material with light emitting characteristics proportional to the partial pressure of the surrounding oxygen [7]. The method is specific to oxygen, as the photoluminescent effects are a result of an oxygen-quenching process and a charge-couple device (CCD) camera is used to capture the variation in light intensity [7]. The pressure information, and thereby the film-cooling effectiveness, is obtained by calibration using four images in different, but specific, conditions [7].

Alongside PSP exists temperature-sensitive paint (TSP) as a similarly non-intrusive but more direct method. It is also a photoluminescent material but the light intensity is proportional to temperature rather than pressure. Images are captured using a CCD camera as well, and calibrated results, generally of high resolution, are obtained by normalising against a reference image with no flow [8].

2.2 Current Techniques for Gas Analysis

Observation of physical fluid flow allows for further study into areas such as sealing effectiveness. Clark et al. achieve this with the use of CO₂ as a tracer gas [9]. The tracer gas is injected upstream and samples are taken at various locations along the system, with the concentration of the tracer gas at each sample location being measured by a gas analyser [10]. Such gas analysers often operate by

optical methods such as infrared (IR), as is the case with the study by Clark et al., where the variation in IR absorption is correlated to CO₂ concentration [9].

2.2.1 Non-Dispersive Infrared Gas Sensing

Specifically, this method of gas analysis is known as non-dispersive infrared (NDIR) gas sensing. As implied in the name, NDIR does not require optical dispersion of IR radiation, omitting the need for dispersive elements such as diffraction gratings [11]. The NDIR technique is fundamentally simple—a source emits IR radiation, interacts with the gas and the results are obtained by comparing the transmitted IR radiation. The results provide both quantitative data on concentration, as well as qualitative data on the gases present [11]. Relative to other gas analysis systems, NDIR, as well as optical methods in general, have good selectivity and sensitivity [3]. However, sophisticated optical components still pose a challenge in the form of high costs [11]. In addition, response times still remain in the region of minutes, with a study by Yasuda et al. finding response times of ≈ 3 min for commercial NDIR CO₂ sensors [12].

2.2.2 Electrochemical Gas Sensing

Electrochemical gas sensing is another common form of gas analysis. The method works by chemical reaction of the target gas, followed by measurement of the induced current which would be proportional to the gas concentration [13]. Similar to NDIR sensors, the measured current is then post-processed to obtain both quantitative (concentration) and qualitative results for the target gas. Whilst electrochemical gas analysis is simple in nature and allows for low cost as well as good sensitivity and selectivity, liquid-electrolyte electrochemical gas sensors experience electrolyte evaporation and solid-electrolyte sensors are held back by limited lifetime [14]. Most significantly, a study by Wan et al. quotes a measurement time in the order of 10² s [14] which is too long for most turbomachinery applications.

2.2.3 Calorimetric Gas Sensing and Gas Chromatography

Other gas analysis methods include calorimetric sensing, which measures the heat generated from combustible gases to quantify its concentration, as well as gas chromatography. Calorimetric sensors are advantageous with their low costs and small size [15], however, they still suffer from insufficient measurement frequency, with response times of 10 s to 15 s for commercial devices [15]. On

the other hand, gas chromatography exists as a high cost and logically complex form of gas sensing. Despite its excellent selectivity and sensitivity [3], analysis generally takes minutes to complete [16].

2.3 Thin-Film Gauges

Whilst all of the above methods hold their respective advantages and disadvantages, it is clear that no method executes measurements at a frequency sufficient for turbomachinery purposes. Thin-film gauges (*Fig. 2.1*) provide an alternative to gas analysis through a heat transfer approach.

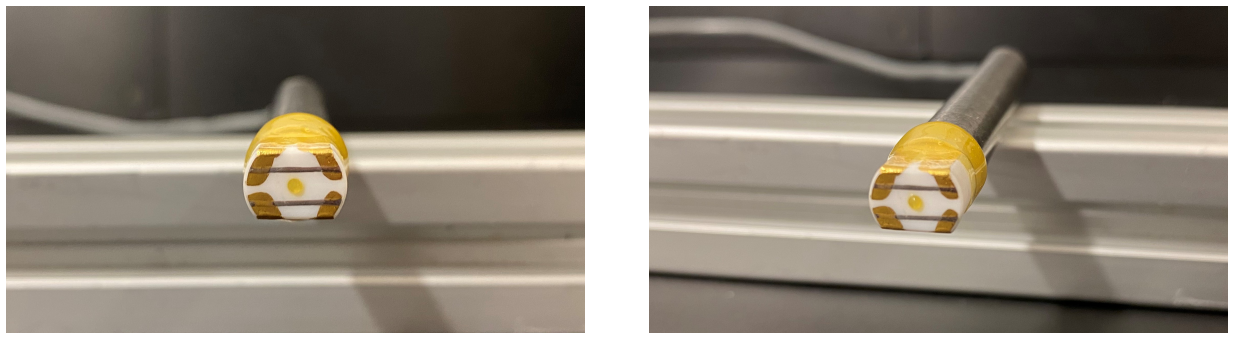


FIGURE 2.1: A thin-film gauge developed and manufactured by Proxisense, consisting of two thin-film circuits.

2.3.1 Principle

Thin-film gauges are conceptually simple—a microthin film of metal is laid on top of a non-conductive base, and the change in temperature is obtained through various methods. These include the use of PSP or TSP, as well as surface thermocouples [17]. Regardless of the method, however, the principle remains largely consistent, and in this report the focus will be on a resistance-based approach to quantifying the temperature change.

The resistance of a system, a thin-film in this case, varies proportionally with temperature as follows, where α is the temperature coefficient of resistance (TCR):

$$R = R_0(1 + \alpha\Delta T). \quad (2.1)$$

Under constant current conditions and using $V = IR$, Equation 2.1 can be converted to:

$$V = V_0(1 + \alpha\Delta T), \quad (2.2)$$

which can be rearranged such that:

$$\Delta T = \frac{\Delta V}{V_0\alpha}. \quad (2.3)$$

As shown, it is a relatively simple method of determining the temperature change using the setup's TCR. The TCR is unique for every setup and is obtained by water bath calibration, which will be explained later in this report.

2.3.2 Sensor Structure, Construction and Manufacturing

A thin-film must be thin enough so as not to affect the temperature history of the base underneath, nor to contribute significant additional mass [17]. Essentially, the effects of the thin-film on the base must be negligible. As such, the microthin layer of metal is sensitive and the construction of a thin-film gauge requires attention to detail.

In terms of the material, nickel and platinum are commonly used for thin-films. Platinum in particular possesses desirable properties, as it remains relatively inert in oxidising surroundings [17]. The film is initially deposited onto the substrate as a liquid containing "fine metallic particles in suspension and chemical agents which lightly attack the surface of the substrate to give a high adherent film" [17]. Whilst the deposition technique will only be described in this report on a fundamental level, note that it is a sensitive process and good practice should be followed in optically polishing and degreasing the substrate surface. Upon deposition, the film and substrate are heated in a furnace for up to 1.5 h, at a temperature dependent on the substrate material, but in the region of 650 °C to 680 °C [17]. The substrate is cooled in the furnace and rapid quenching should be avoided as it results in internal stresses [17]. This painting and firing process is generally repeated to build up the thin-film until a final thickness of 0.1 µm to 1.0 µm [17]. In case of unstable resistance during use of the thin-film, the gauge can be annealed to reduce such instability by heating at 160 °C for 12 hours [17].

It must also be ensured that the thin-film can be easily attached to electrical leads, which themselves should be thermally and electrically inert [17]. The electrical leads must be of as low resistance as possible, so are often constructed with significant width and occasionally increased thickness as well. The thickness, however, must not interfere with the boundary layer for applications in fluid flow experiments [17]. With regards to material, gold and copper are two of several materials used for electrical leads.

This conventional method of thin-film manufacturing is labour-intensive and the resultant device is inevitably large due to wide electrical leads. The width can be reduced by either increasing the

thickness or shifting to a four-wire measurement system. The four-wire system, however, introduces additional and undesirable complexities [18]. As such, Collins et al. developed a novel thin-film fabrication technique to maximise the electrical lead thickness by "etching a pre-laminated sheet of copper and polyimide using a dry film photoresist" [18]. The process has resulted in the production of smaller and more robust thin-film gauges compared to conventional methods [18].

2.4 Thin-Film Gauge Heat Transfer Measurements

Thin-film technology has historically been used in various applications, particularly in the field of aerospace due to its minimally intrusive nature and ability to operate in hostile environments [19]. It was first utilised to capture heat transfer in shock tunnels [18], and is still used for the same application to this day [20]. Thin-film gauges are also widely used to measure heat transfer in film cooling [21] and nozzle guide vanes [22].

2.4.1 Measurements by Thermal Product

A novel application of thin-film was developed by Chana [23] in detecting the contamination of oil and fuel. The method makes use of the thermal product principle introduced in Chapter 1 to measure the concentration of contaminants up to a sensitivity in the order of 0.01 % or 10 PPM [23]. The working principle is that the thin-film is pulsed with a step change, generating heat in the metal film, and the heat transfer between the film and its surroundings is quantified. The heat transfer is dependent on the thermal product of the surrounding, which in itself varies with the concentration of contaminants in the surrounding fluid [23].

2.4.2 Application to Gas Sensing: MEMS Thin-Films

This concept can also be applied to gas sensing, where the heat transfer is influenced by the thermal product of the gas, or mixture of gases, surrounding the thin-film. However, as thermal product variations in gases are of significantly smaller magnitude than that of liquids, this report looks to combine thin-film technology with MEMS to achieve sensitivities sufficient to detect gas composition. Flusso Ltd. has developed the world's smallest flow sensor [24], which senses flow rate using a small-scale thin-film. On a fundamental level, two tungsten resistors are embedded: one for flow anemometric-based measurements and the other for temperature compensation [24]. Gas flows through the sensor and power is passed through the anemometric resistor so as to maintain a

constant temperature of 230 °C. The power required to maintain the constant temperature is tracked and post-processed to obtain results for the flow, such as flow rate and fluid velocity [24]. This report studies the possibilities of adapting such a sensor for gas sensing purposes, potentially allowing for a high frequency and low cost solution to the gap in current gas analysis technologies.

3 Research Question

This report examines the research question, "How could we exploit thin-film and MEMS technologies to measure gas composition at high frequencies?"

Thin-films present a novel method of gas analysis by quantifying the varying thermal product of its surroundings. MEMS devices operate at high frequencies, and their miniaturised size allows for increased sensitivity to heat transfer.

We start by studying a handheld thin-film gauge manufactured by Proxisense, a spin out from the University of Oxford [25]. The device is currently used in a wide range of fields including pharmaceutical, aerospace, oil & gas and power generation. Specifically, it is used to detect contamination and degradation levels in fuel and pharmaceutical production [26]. It can also identify counterfeit drugs and vaccines [26], and more recently has been used to detect skin cancer. The Proxisense sensor will be used to gain a better initial understanding of implementing heat transfer as a method of identifying materials through thermal product. A 1D semi-infinite model will be used to capture the heat transfer of the thin-film gauge.

We explore further with a MEMS gas flow sensor manufactured by Flusso Ltd. [27], a spin out from Cambridge University. As a low cost but accurate solution to flow sensing, its applications include smart inhalers, industrial pneumatics & automation, as well as aerial drones and household electronics [28]. The MEMS sensor outputs reliable and robust data on mass flow, volumetric flow, air speed and differential pressure [28]. Due to its microthin internal structure, the device allows for increased sensitivity, improved SNR and higher frequency relative to the Proxisense thin-film gauge. The Flusso sensor will be used to further investigate the use of thin-films to capture heat transfer for gas sensing by exploiting the high frequency and high sensitivity nature of MEMS technology.

4 Experimental Methods

4.1 Experimental Setup

As both the Proxisense sensor and the Flusso sensor operate on the same fundamental thin-film principle, they are largely operated the same way experimentally. The sensors are connected to a Proxisense control box (*Fig. 4.1a*), serial number 3103A003, via a 9-pin D-sub connector (*Fig. 4.1b*). The control box itself is connected to a computer via two USB Type A to USB Micro B cables, one of which serves to power the system and the other to transmit data. The system is run by software developed by Proxisense, that allows the user to input settings for the control box to drive step currents to the sensor. The software interface is as shown in Figure 4.2 and allows the step currents to be customised with the following settings:

1. Pulse current. For each of two channels that the control box can pulse, this sets the magnitude of the current for the step current.
2. Sample rate. This is the frequency of data recording and can be increased up to a maximum of 4.8 kHz for the control box used in this project.
3. Pulse length. The number of samples to run a step current for. For example, 24 samples at 4.8 kHz would equate to $\frac{24}{4800} = 5 \text{ ms}$.
4. Pulse repeat rate. The length of interval between consecutive pulses. This is important as systems need sufficient time to return to their original state, at ambient temperature, after being pulsed.
5. Pulse count. How many pulses to execute in one run.

N.B. Bias length, output start and output length influence data collection lengths and start points. Target voltage and target % window are for calibration purposes and are not significant for general pulsing purposes.



(A) Proxisense control box.

(B) Entire setup including Proxisense thin-film sensor.

FIGURE 4.1: Identification of the starting point to omit starting processes.



FIGURE 4.2: User interface of Proxisense software.

4.2 Data Collection

With the sensor, control box and computer all connected, the sensor is exposed to the testing fluid and the setup is ready to run experiments. Using the software, a set number of pulses of constant current are executed in intervals. These settings vary depending on the sensor that is in use. Note that, whilst the pulses are of constant current, this is not equivalent to constant power since the resistance of a thin-film increases as the sensor heats up through pulsing and $P = I^2R$. During pulsing, the voltage across the thin-film is measured and recorded at a set sample rate.

Data is recorded by the software and output as a CSV file containing both the settings used and voltage data points. As data is captured from several sample points before the start of the pulse, the starting point of the pulse must first be identified from the obtained data. By plotting the measured voltage against time, the starting point can be identified as the first data point at which spacing between consecutive sample points become consistent. Figure 4.3 visualises this procedure for clarity and demonstrating the omission of the effects of starting processes present due to the nature of the pulsing method. Such starting processes occur when stepping up to the desired current of the pulse.

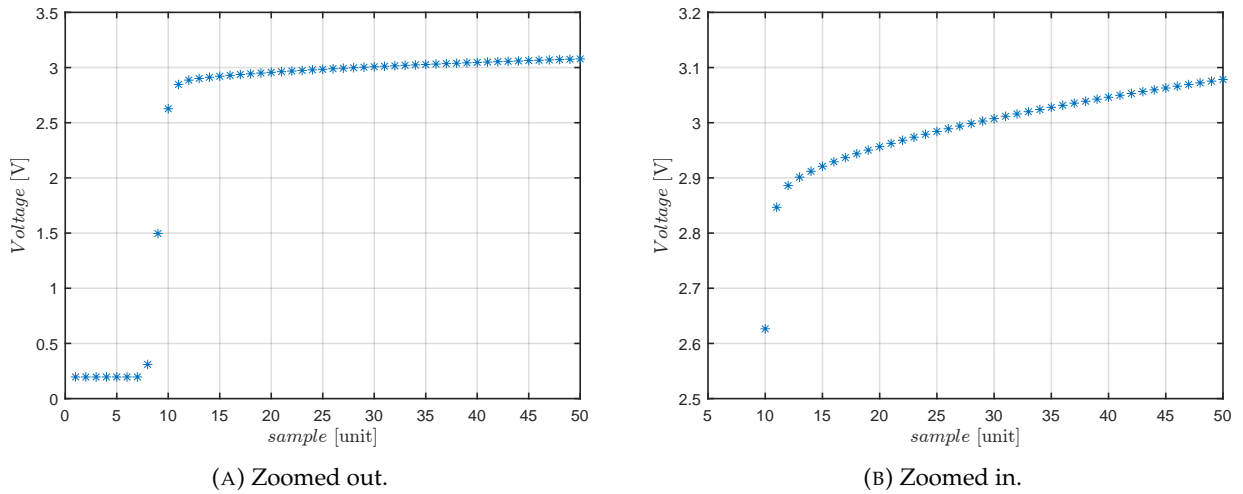


FIGURE 4.3: Identification of the starting point to omit starting processes. In this experiment, the 11th data point is taken as the starting point.

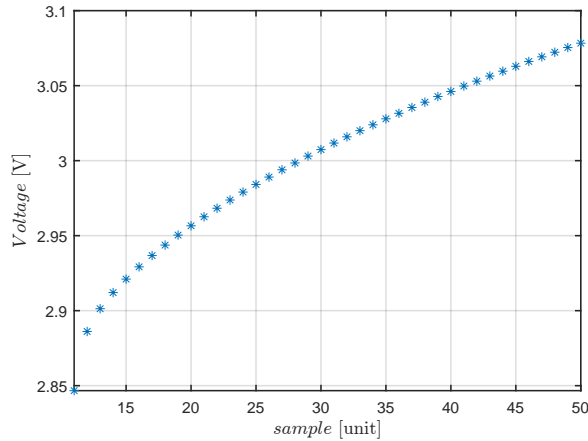


FIGURE 4.4: Final curve after omitting starting processes.

Figure 4.4 shows the curve after the starting process is omitted. The starting point is generally consistent for a single sensor but varies between sensors. For example, the starting point for the Proxisense sensor is the 11th data point but the starting point for the Flusso sensor is the 5th data point. The Proxisense sensor is significantly larger in size, inevitably requiring a longer duration for the step current to run through the system and reach starting equilibrium. This results in starting processes of larger time scales.

4.3 Water Bath Calibration

With the starting point identified, the starting voltage, V_0 , can also be identified. All other voltages are taken relative to V_0 and Equation 2.3 can be applied to obtain the temperature change. This, however, is almost entirely dependent on the TCR of the thin-film. Whilst TCR values are available

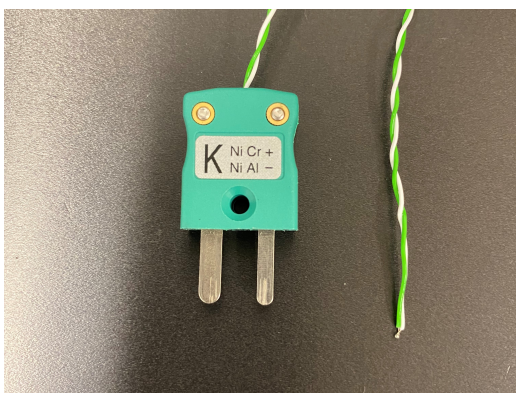


FIGURE 4.5: K-type thermocouple.

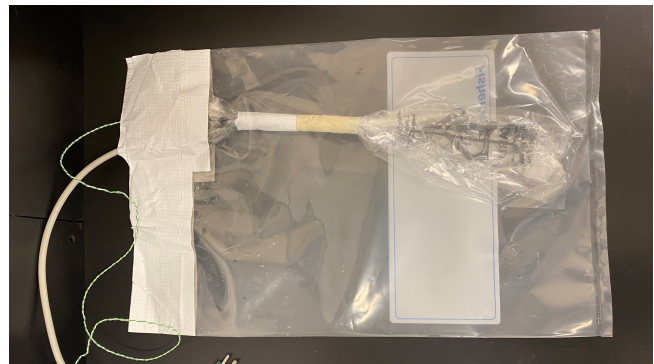


FIGURE 4.6: Proxisense sensor made water-tight with two layers of plastic sleeves.

in literature for bulk materials, the value can vary depending on the size and structure of the thin-film. Therefore, it is critical that the TCR is determined for each unique system—this is done through a water bath calibration.

4.3.1 Principle

The principle of water bath calibration relies on measuring the resistance of two nodes within the system as the temperature is varied. Water baths allow the temperature variation to be carried out in a stable and consistent manner, although the approach does limit testing to temperatures in the liquid phase of water, 0 °C to 100 °C.

Water bath calibrations for both the Proxisense and Flusso sensors were conducted. First, K-type thermocouples (*Fig. 4.5*), made with a thermocouple welder, were attached as close to, but not in contact with, the thin-films as possible. The thermocouples were secured using Kapton® Tapes (*Fig. 4.7*). The Kapton® material isolates the thermocouple from surrounding air so that the temperature measurement is solely that of the sensor. The sensors were then wrapped in two layers of plastic sleeves—one thin internal layer and one thicker external layer, both respectively secured at the top to provide water-tight seals (*Fig. 4.6*). This was particularly important for the Flusso sensor, as the sensor was prone to water damage due to its design as a gas flow sensor.

The water bath contained two thermocouples along with one internal temperature sensor, meaning 5 measurements were made simultaneously: three temperature readings at different locations in the water bath, one temperature reading at the sensor itself and one resistance reading across the sensor thin-film. For the calibrations, several settings were adjusted to ensure results were of maximum



(A) Top view.

(B) Diagonal view.

FIGURE 4.7: Thermocouples secured onto each side of the Proxisense sensor's MA-COR® substrate using Kapton® tape.

accuracy and reliability whilst completing the calibrations in reasonable time. Water bath calibrations can take multiple days to complete.

4.3.2 Settings and Procedure

For calibrations of both sensors, identical settings and procedures were followed. Between a range of 35 °C and 50 °C, measurements were taken at 5 K intervals. Three cycles were conducted, where one cycle consists of measurements from 35 °C up to 50 °C and back down to 35 °C. Ideally, a larger range starting from room temperature (≈ 25 °C) would have been studied, however, the cooling system had malfunctioned and each cycle would have taken days due to slow natural cooling of the large body of water. In addition, there were settings to ensure thermal equilibrium at each measurement temperature, which were as follows:

1. Bath temperature tolerance: 0.8 K. This is the tolerance for the temperature difference between the set bath temperature (35 °C, 40 °C, 45 °C or 50 °C) and the average of the two water bath thermocouples.
2. Bath internal temperature tolerance: 0.2 K. This is the tolerance for the temperature difference between the set bath temperature and the water bath internal temperature sensor.
3. Specimen temperature tolerance: 1.0 K. This is the tolerance for the temperature difference between the set bath temperature temperature and the thermocouple on the specimen (thin-film).
4. Convergence monitoring time period: 3 min. This is the minimum duration for which the above conditions must be continuously held for a measurement to be taken.

5. Bath temperature convergence tolerance: 0.4 K. This is the tolerance for the temperature variation throughout the convergence monitoring time period, for all four temperature measurements.

4.3.3 Results: Flusso MEMS Sensor

The Flusso sensor returned a very linear temperature-resistance relationship. As seen in Figure 4.8, the line of best fit overlays well on the data points, all within error bars, with an R^2 value of 0.999. The gradient and y-intercept are found to be 0.275 and 121.840 respectively. Rearranging Equation 2.1, it is possible to determine the sensor's TCR, α :

$$\alpha = \frac{\frac{R}{R_0} - 1}{\Delta T} = \frac{\Delta R}{R_0 \Delta T} = \frac{\text{grad}}{\text{y-intercept}}, \quad (4.1)$$

For the Flusso sensor, this evaluates to $2.257 \times 10^{-3} \text{ K}^{-1}$. In the literature, the TCR for tungsten in bulk is quoted as $4.5 \times 10^{-3} \text{ K}^{-1}$ [29]. The two values are in the same order of magnitude, and the discrepancy appears to be due to the differences in shape and size between bulk tungsten and the Flusso sensor's tungsten filament.

4.3.4 Results: Proxisense Thin-Film Gauge

The Proxisense sensor, on the other hand, showed less linear results (Fig. 4.9), exhibiting effects of hysteresis. Hysteresis is a general phenomenon relating to a "characteristic looping behaviour of the input-output graph" [30]. Specifically, with the water bath calibration, the resistance across the Proxisense thin-film appears to vary at different rates depending on whether the temperature is rising or descending. Whilst further study is required to pinpoint the multiple factors contributing to this effect, one likelihood is that it is due to a lack of annealing during the manufacturing process. Another possibility is that it may be due to imperfections in the joints between the platinum thin-film and gold circuit. Considering their different thermal properties, and the sensitive nature of thin-film manufacturing, it is challenging to eliminate such flaws.

Despite the hysteresis, the method of TCR calculation remains identical to that of the Flusso sensor. Applying linear regression to the data yields a gradient and y-intercept of 0.0029 and 3.3678 respectively. The R^2 value of the line of best fit is 0.777. Applying Equation 4.1 returns a TCR of $8.611 \times 10^{-4} \text{ K}^{-1}$, which is comparable to the bulk platinum value in the literature of 3.927×10^{-3}

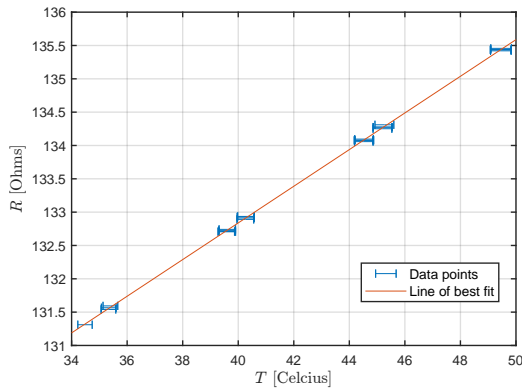


FIGURE 4.8: Water bath calibration of Flusso sensor. Errors bars represent the 0.75 % uncertainty of the K-type thermocouple.

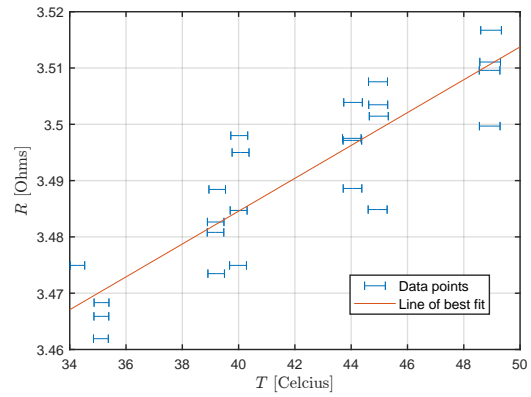


FIGURE 4.9: Water bath calibration of Proxisense sensor. Errors bars represent the 0.75 % uncertainty of the K-type thermocouple.

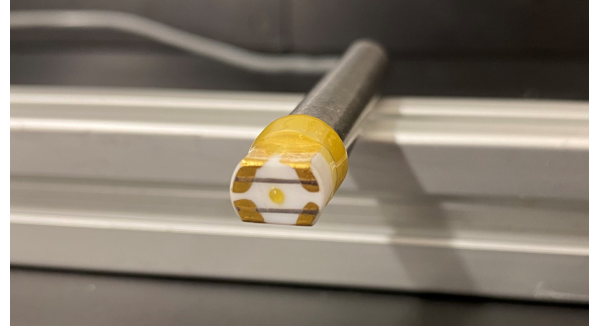
K^{-1} [29]. Again, this variation can be attributed to the differences in size and shape between bulk platinum and the Proxisense sensor's platinum thin-film.

5 Proxisense Thin-Film Gauge

The Proxisense sensor is a handheld device consisting of two thin-film circuits (*Fig. 5.1*). The substrate is made of MACOR®, a type of glass ceramic, and the thin-films are made of platinum. During manufacturing, they are deposited thicker than required and hand-polished to increase the resistance up to 3.44Ω . They are connected to the rest of the sensor by a gold circuit of negligible resistance.



(A) Front view.



(B) Diagonal view.

FIGURE 5.1: Proxisense thin-film gauge, displayed again for reference.

5.1 1D Model

5.1.1 Derivation

The heat transfer of this sensor can be captured by a 1D model (*Fig. 5.2*) since the MACOR® substrate can be assumed to be a semi-infinite solid. The model can be derived [31] by starting with the unsteady heat transfer equation in 1D, where $T(x, t)$ is temperature, x is distance into substrate, t is time and $\beta = \frac{k}{\rho c_p}$:

$$\frac{\partial^2 T(x, t)}{\partial x^2} = \frac{1}{\beta} \frac{\partial T(x, t)}{\partial t}. \quad (5.1)$$

This can be solved by Laplace transform, where $T(x, 0) = T_0$ and $T(0, t) = T_s$:

$$\frac{T(x, t) - T_0}{T_0 - T_s} = \operatorname{erf} \frac{x}{2\sqrt{\beta t}}. \quad (5.2)$$

Fourier's law of thermal conduction states that the heat flux density, $q(x)$, can be given by:

$$q(x) = -k \frac{\partial T}{\partial x}. \quad (5.3)$$

Taking the partial differential of Equation 5.2 leads to:

$$\frac{\partial T}{\partial x} = \frac{T_0 - T_s}{\sqrt{\pi\beta t}} \exp \frac{-x^2}{4\beta t}. \quad (5.4)$$

Combining and rearranging Equations 5.2, 5.3 & 5.4 gives:

$$T - T_0 = \frac{2q_s \sqrt{\frac{\beta t}{\pi}}}{k} \exp \frac{-x^2}{4\beta t} - \frac{q_s x}{k} \left(1 - \operatorname{erf} \frac{x}{2\sqrt{\beta t}}\right). \quad (5.5)$$

As it is sufficient to observe the temperature of the thin-film at the surface, take the solution at $x = 0$ and substitute $\beta = \frac{k}{\rho c_p}$:

$$T = T_0 + \frac{2q_s}{\sqrt{\pi} \sqrt{\rho c_p k}} \sqrt{t}. \quad (5.6)$$

Due to the symmetry of the model, it is possible to obtain temperatures on either side of the thin-film (fluid or substrate). Whilst the two problems do collapse into one at the surface, one must still choose to study either the fluid side or the substrate side in order to reach a full solution. The following solution takes the fluid approach (q_{in} is the total heat flux into the system by the thin-film):

$$q_{in} = q_{fluid} + q_{substrate}, \quad (5.7)$$

$$q_{fluid} = q_{in} \cdot \frac{\sqrt{\rho c_p k}_{fluid}}{\sqrt{\rho c_p k}_{fluid} + \sqrt{\rho c_p k}_{substrate}}, \quad (5.8)$$

$$T_{fluid} = T_0 + \frac{2q_{fluid}}{\sqrt{\pi} \sqrt{\rho c_p k}_{fluid}} \sqrt{t}. \quad (5.9)$$

Substituting Equation 5.8 into Equation 5.9 yields:

$$T_s = T_0 + \frac{2q_{in}}{\sqrt{\pi} (\sqrt{\rho c_p k}_{fluid} + \sqrt{\rho c_p k}_{substrate})} \sqrt{t}. \quad (5.10)$$

The final solution at the surface (Eq. 5.10) considers the different heat flux on the fluid side and the substrate side. It is important to highlight two key takeaways. First, the temperature change, $T - T_0$, is proportional to the square root of time—a \sqrt{t} shape should be expected of the heat curve when pulsing the Proxisense sensor. Second, the gradient of $T - T_0$ plotted against \sqrt{t} is inversely

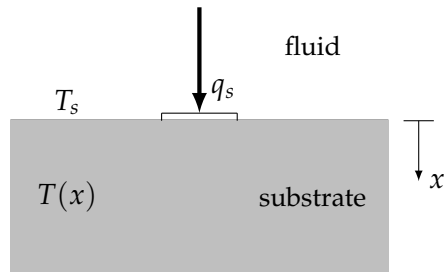


FIGURE 5.2: 1D semi-infinite model, visualised at the cross-section of a thin-film structure. Note that, in this specific case, q_s represents heat flux into the substrate.

proportional to the sum of the thermal products of the fluid and the substrate. This means that the heat curve is affected solely by the two thermal products, as the other terms involved in the gradient are constants.

5.1.2 Limitations

The 1D model is simple, which also means it inevitably fails to capture some of the heat transfer processes involved when pulsing the Proxisense sensor. Due to its one-dimensional nature, it assumes zero convection in the fluid and ignores the lateral conduction of the driving electronics in the solid substrate. This limits the model's use to small time scales where such assumptions can be reasonably made. The theoretical model also omits real-life phenomena such as starting processes, which introduces the need to manually determine the starting point, as demonstrated in Chapter 4. The substrate must also be of one single material, and of sufficient size and depth to maintain the semi-infinite assumption.

Despite these limitations, it was determined that the assumptions could reasonably be applied to the Proxisense sensor and its pulsing method. The MACOR® base is uniform and deep enough for the semi-infinite assumption and the pulsing is of a time scale small enough to omit effects due to convection and lateral conduction.

5.1.3 Alternative Options of Modelling

Beyond the 1D model, there were several other options for modelling the Proxisense sensor, including commercial finite-elements codes such as ANSYS [32]. ANSYS is "a general-purpose finite-element modeling package for numerically solving a wide variety of mechanical problems" [33]. These include structural, heat and fluid problems, but also extend to acoustic and electromagnetic problems [33]. Solutions to such problems are generally obtained through three main steps [33]:

1. Define the problem: define the geometry of the object and its material properties, as well as the mesh.
2. Specify boundary conditions: assign loads, constraints, thermal conditions, etc.
3. Solve and view results: displacements, stress distributions, temperature maps, etc.

Thermal analysis of the Proxisense sensor using ANSYS would have had its own advantages and disadvantages. ANSYS simulation allows the user to specify the exact geometry of an object by importing CAD files. With accurate geometries, ANSYS's finite-elements method would have captured minute details of the heat transfer taking place, including fluid convection and lateral conduction. However, such advantages are the result of additional complexities. Defining the problem requires more effort, such as creating CAD models of the sensor. The required computational power and duration are also significantly larger. Furthermore, in the case that tuning is required, the extra intricacies in geometric variations and material properties may lead to difficulties. The tuning of low-order models is significantly easier.

For the purpose of understanding the concept of thin-film, the 1D model was found to have sufficient accuracy and gives good insight into the key physics and design sensitivities. The simple structure and large size of the Proxisense sensor combined with the pulsing method's small time scale to realise experimental conditions similar to that of the 1D semi-infinite heat transfer model in Figure 5.2.

5.2 Experimental Procedure

The experimental procedures for the Proxisense sensor are as detailed in Chapter 4. The pulse current was varied between experiments, from 200 mA to 400 mA. The suggested limit was 400 mA as there was risk of breaking the thin-film line due to its fragility. The sample rate and pulse length were set to 4.8 Hz and 800 sample (≈ 167 ms) respectively. Due to its significant size and the MACOR® material's high heat retention property, the pulse repeat rate was set at a generous 10 s. 10 pulses were executed each run.

The experimental setup was as shown in Figure 5.3. A stand and clamp was used to hold the sensor still, sufficiently submerged in a beaker of deionised water. Deionised water was used as the fluid, since its thermal product is well-documented in the literature, as well as for logistical reasons. Furthermore, liquids were preferred to gases as they possess significantly higher thermal products and therefore retain more heat from the thin-film, keeping overall temperatures lower. As a reference,

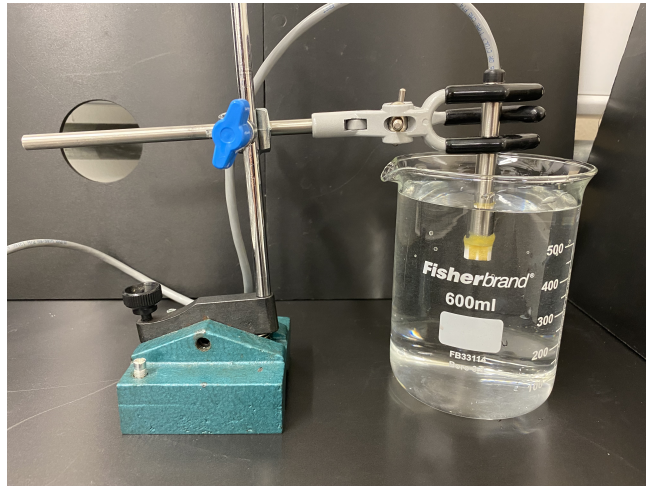


FIGURE 5.3: Experimental setup of the Proxisense sensor in deionised water.

the thermal product of air at 300 K was calculated in Chapter 1 as 5.6295, whereas the thermal product of water is 1595.0 [34]. For MACOR® at 25 °C, $\rho = 2520 \text{ kg m}^{-3}$, $c_p = 790 \text{ J kg}^{-1} \text{ K}^{-1}$ and $k = 1.46 \text{ W m}^{-1} \text{ K}^{-1}$ [35]. This equates to a thermal product of 1704.9.

5.3 1D Model Validation

The Proxisense sensor was pulsed 26 times at 300 mA for 167 ms in 10 s intervals. All 26 pulses were converted to temperature using Equation 2.3, and the standard deviation was calculated for every data point. Figure 5.4 shows the experimental data on a temperature-time plot. Figure 5.5 shows the same data, except the temperature is plotted against the square root of time for better comparison with the 1D model, which is linear against \sqrt{t} . As seen on the figures, the 1D model holds well against experimental data until approximately 30 ms. This is expected because, beyond a certain point, several assumptions imposed in deriving the model begin to break down. For example, there comes a point where the sensor begins to observe convection in the fluid and lateral conduction in the substrate. Note that there are slight misalignments between the experimental data and the 1D model at early times which is due to starting processes as explained earlier.

5.4 1D Model Predictions

5.4.1 Air-CO₂ Mixture

With the 1D model validated against experimental data up to 30 ms, it is possible to predict fluids with different properties—i.e., the model can be run to predict the response with other fluids,

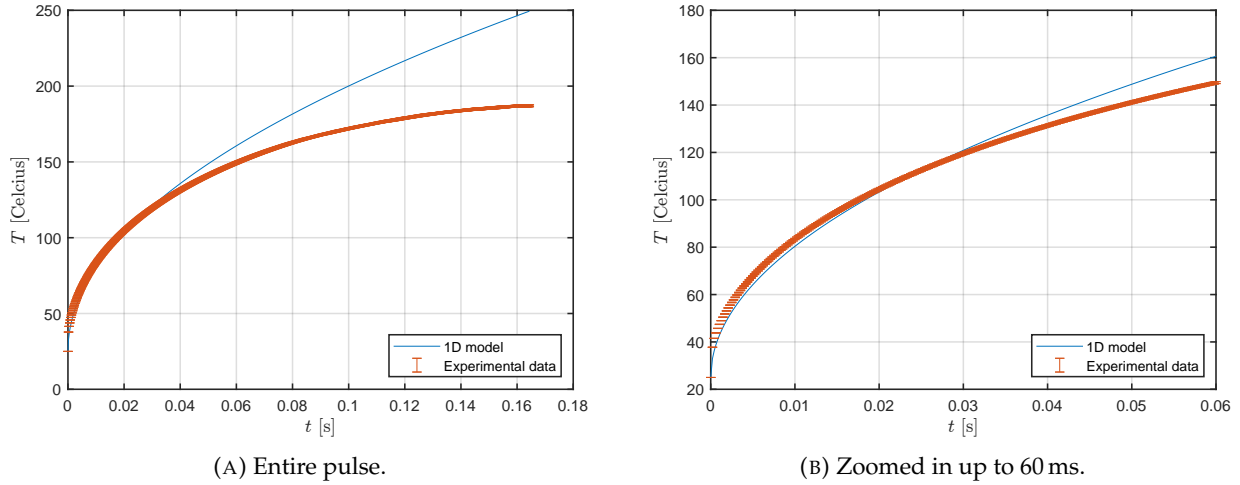


FIGURE 5.4: Temperature plotted against time from pulsing of Proxisense sensor with 300 mA step currents of length 167 ms, alongside comparison with 1D model prediction. Error bars for all plots in Section 5 were placed at one standard deviation from the data point.

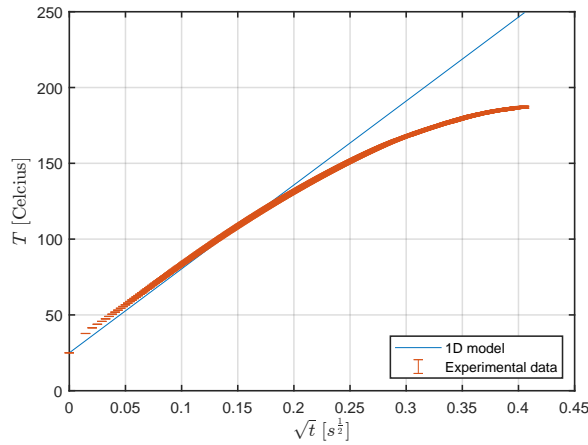


FIGURE 5.5: Temperature plotted against square root of time from pulsing of Proxisense sensor with 300 mA step currents of length 167 ms, alongside comparison with 1D model prediction.

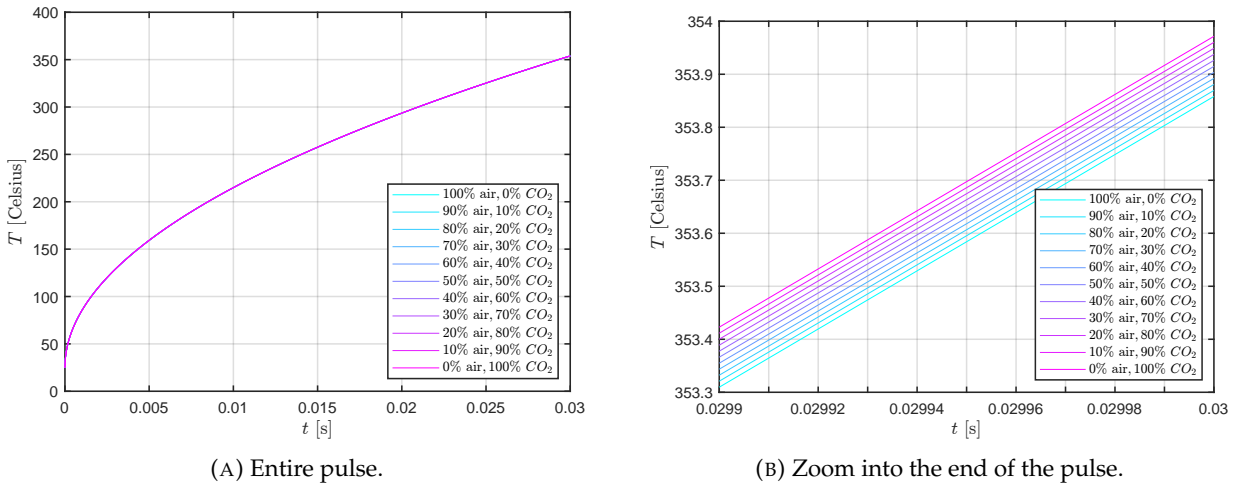


FIGURE 5.6: 1D model prediction of a range of compositions of an air-CO₂ mixture.

with gases being of particular interest. Simulations were first run for a mixture of air and CO₂ for a range of compositions in 10% intervals. The pulse length was set to 30 ms as that was the maximum duration for which the 1D model held up against experimental data, and the current was set to 400 mA to maximise the final temperature differences. As seen in Figure 5.6a, the difference between each composition is practically invisible when viewing the entire pulse length. When zooming into the very end of the pulse (Fig. 5.6b), where the differences are largest, it is possible to see the exact temperature differences that separate the compositions. Even so, the model prediction shows that experiments for 100% air and 100% CO₂ only vary by 0.114 K, equivalent to a 0.0322 % difference. Such temperature variations will not be able to be differentiated from signal noise—it is safe to say that, in this experiment, the Proxisense sensor would not be able to identify the gases. Also note the significant increase in temperature relative to experiments with water, even whilst considering the 33.3 % increase in current. With a pulse length under a fifth of that of the water experiments, the temperature rise would be approximately 2.6 times larger. This may be a limiting factor for some sensors depending on their maximum operating temperature.

5.4.2 Enhancing Temperature Differences

There are several ways to enhance the temperature difference beyond looking at the raw difference at the end of the pulse. Rather than simply looking at the difference in the Celsius scale, taking the difference from the starting temperature will return a slightly larger change. However, such a change would see minuscule effects, particularly for this Proxisense sensor in these operating conditions, since the starting temperature is very small compared to the temperature difference. Another approach would be to calculate the differences in gradient. However, the most effective method is to

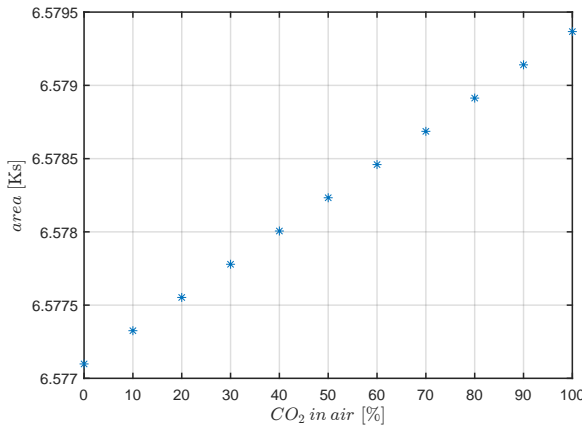


FIGURE 5.7: Integral of the air-CO₂ heat curves in Figure 5.6.

obtain the integral of the heat curves. Figure 5.7 is the result of the area integral process, displaying the area under each of the curves in Figure 5.6. With the area integral method, the temperature difference increased to 0.0345 %, which is a slight improvement from the initial method. However, it is still insufficient to differentiate between different gases.

5.4.3 Air-Argon Mixture

As mentioned in Chapter 1, the thermal product difference between argon and air is larger than that between CO₂ and air. Simulations were run to investigate the greater thermal product difference between argon and air, and the results are presented in Figure 5.8a. Once zoomed into the end of the pulse (*Fig. 5.8b*), it is noticeable that the temperature differences are larger than those of Figure 5.6b. Quantitatively, the difference between 100 % air and 100 % argon after 30 ms is 0.339 K. This equates to a percentage difference of 0.0958 %. On the other hand, using the area integral approach, a percentage difference of 0.103 % is obtained. Whilst both of these values are significantly larger than that of the air-CO₂ experiments (*Fig. 5.6*), they are still insufficient for gas differentiation purposes.

5.5 Improvements for Increased Sensitivity

The 1D model can be used to explore potential changes to increase these temperature differences. It is obvious that increasing the overall temperature change, $T - T_0$, leads to a larger temperature difference between varying gases at the end of the pulse. By looking at Equation 5.10, it is possible to see another simple way to achieve this—increasing the heat flux, q_{in} , which can be attained by increasing the power input or decreasing the filament area. However, it is more desirable to enhance the temperature difference relative to the magnitude of the overall temperature change. Therefore, it

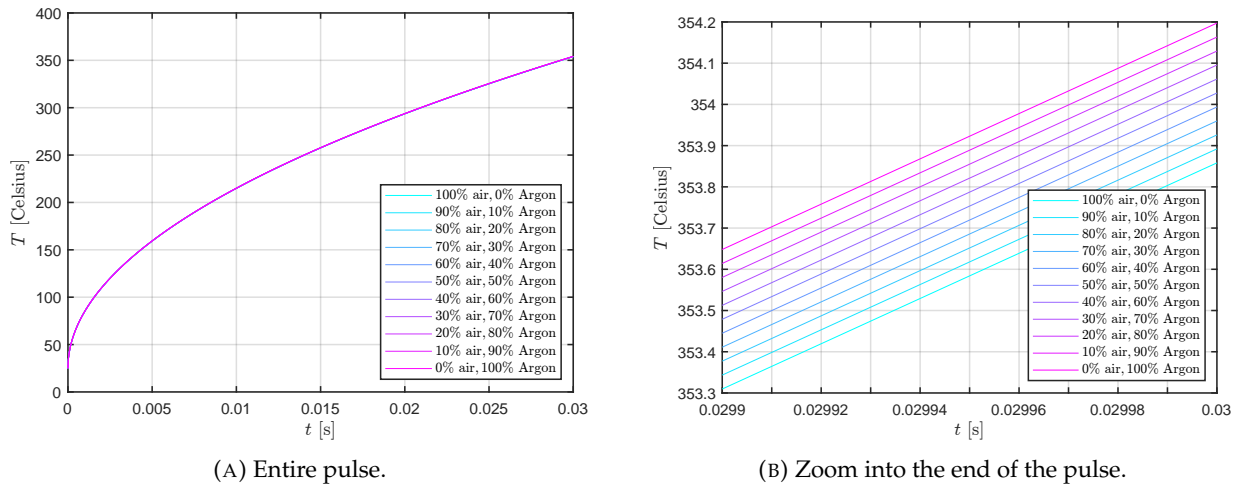


FIGURE 5.8: 1D model prediction of a range of compositions of an air-argon mixture.

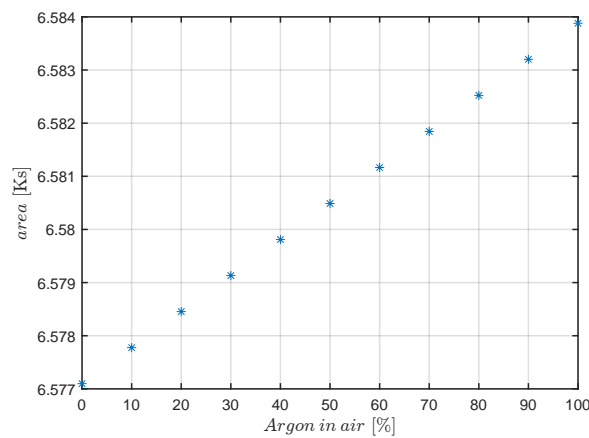


FIGURE 5.9: Integral of the air-argon heat curves in Figure 5.8.

is important to look at the total thermal product term, $\sqrt{\rho c_p k_{fluid}} + \sqrt{\rho c_p k_{substrate}}$, in Equation 5.10. Recall that MACOR®'s thermal product, 1704.9, is significantly larger than that of gases, which are in the region of 3 to 6. Implementing a substrate with a lower thermal product should allow the sensor to become more sensitive to changes in the fluid's thermal product.

As such, it is critical to investigate higher sensitivity alternatives to the Proxisense sensor that builds on its thin-film fundamentals. The Flusso MEMS sensor provides exactly that by utilising the high sensitivity and high frequency nature of MEMS technology whilst retaining the thin-film heat transfer approach to gas sensing. More specifically, the sensor's filament has a significantly smaller area and the thermal product of its substrate is lower—both changes earlier identified as potential improvements to the Proxisense sensor.

6 Flusso MEMS Sensor

The Flusso FLS110 MEMS sensor (Fig. 6.1) is a miniaturised gas flow sensing system which analyses gas flow by implementing two tungsten resistors across the length of the device [24]. The resistors are embedded in a SiO_2 membrane of $4.5 \mu\text{m}$ thickness [24], and they are both of 128.7Ω resistance. The sensor's overall dimensions are $1300 \times 1600 \mu\text{m}$ and the etched membrane has a diameter of $1100 \mu\text{m}$ [24]. The sensor has two operating methods as shown in Figure 6.2. In this project, only the through-flow method was used. Its basic features can be seen in Figure 6.1, where overall structures of the nodes, membranes and resistors, as well as the scale of the sensor's size, are shown.

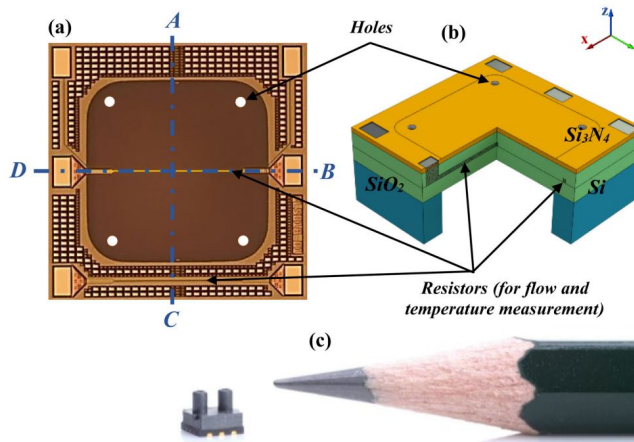


FIGURE 6.1: Basic structure of the Flusso sensor, along with its size scale. Extracted from Figure 1 of Gardner et al. [24].

There are several key differences compared to the Proxisense thin-film gauge. First, the length scale of the Flusso device is an order of magnitude smaller. Second, the resistors are of wire structure

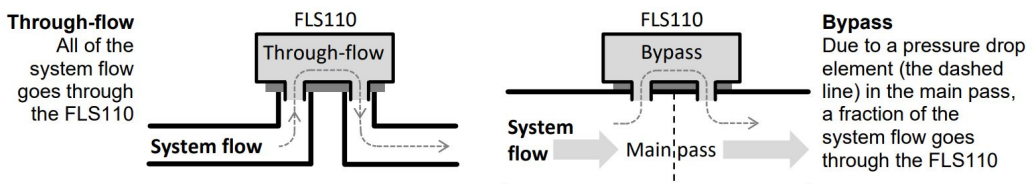


FIGURE 6.2: Two flow configurations of the Flusso mass flow sensor. Extracted from Figure 2 of the FLS110 Miniature Gas Flow Sensor Datasheet [36].

rather than a thin-film. The resistors' interactions with surrounding fluid is also different, as spaces both above and below the wire resistors of the Flusso sensor are occupied by gas. Third, the Flusso sensor's membrane thickness ($4.5\text{ }\mu\text{m}$) is three orders of magnitude smaller, resulting in a completely different pattern of vertical conduction. Finally, the membrane is made of SiO_2 , a material with a smaller thermal product than the Proxisense sensor's MACOR® substrate.

6.1 Network Model

Due to such differences in the physical nature of the Flusso sensor, the 1D model (*Eq. 5.10*) can no longer be applied to capture its heat transfer. Mainly, the small length scale of the device means that heat transfers rapidly throughout the system, which must be accounted for. A two-dimensional finite-elements approach was proposed to model the sensor. By discretising the sensor on a cross section along its length, a network model (*Fig. 6.3*) was developed to reproduce the rapid conduction and convection occurring at each element, capturing effects of heat transfer that were previously ignored by the 1D model used for the Proxisense sensor.

6.1.1 Derivation

For the purpose of utilising the sensor's thin-film properties, it is sufficient to use just one of the two resistors. The middle resistor is chosen to allow for symmetry, somewhat simplifying the modelling process. To start the modelling process, a cross section is taken on a plane orthogonal to the x -axis in Figure 6.1. Due to the microthin nature of the membrane, it is sufficient to assume the thickness as one layer. Figure 6.3 shows the underlying intuition behind the network model. Q_0 represents half the heat entering the system by power input through the resistor—essentially, $Q_0 = \frac{1}{2}I^2R$. The $\frac{1}{2}$ term accounts for the fact that the model considers only one half of the sensor due to symmetry. Note that Q_0 is not constant since temperature rise induces resistance rise, resulting in increased power input during the constant current step. Q_x represents lateral heat transfer by conduction and Q_y represents vertical heat transfer by convection. The assumption is made that the convection above and below the membrane is identical. More precisely, Q_x and Q_y are calculated as follows, where k is the membrane's thermal conductivity and h is the convective heat transfer

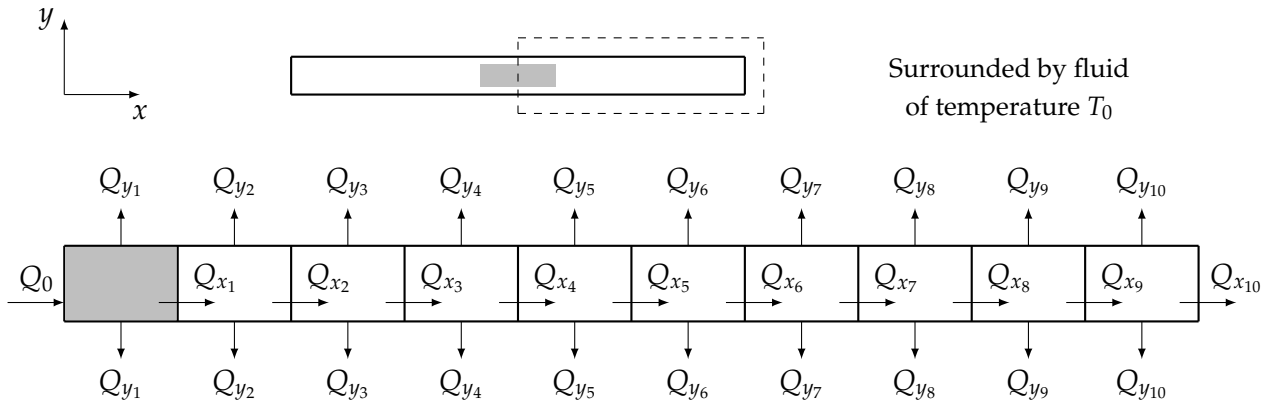


FIGURE 6.3: Finite-elements network model, visualised at the cross-section orthogonal to the x -axis in Figure 6.1. The discretisation is kept low to $n = 10$ for clarity. In the actual MATLAB model, the sensor is discretised beyond $n = 60$.

coefficient:

$$Q_{x_i} = \frac{k\delta y}{\delta x} (T_i - T_{i+1}), \quad (6.1)$$

$$Q_{y_i} = h\delta y (T_i - T_0), \quad (6.2)$$

Incrementally, the total energy transferred during one time step is:

$$dQ = Qdt, \quad (6.3)$$

therefore, the net heat transfer during a given time step is:

$$dQ_{net_i} = (Q_0 - Q_{x_1} - 2Q_{y_1})dt \text{ for } i = 1, \quad (6.4)$$

$$dQ_{net_i} = (Q_{x_{i-1}} - Q_{x_i} - 2Q_{y_i})dt \text{ for } i > 1. \quad (6.5)$$

Converting the energy change to temperature change, with c_p and ρ being the specific heat capacity and density of the membrane, respectively, yields:

$$dT_i = \frac{dQ_{net_i}}{c_p \delta m} = \frac{dQ_{net_i}}{c_p \rho \delta x \delta y}, \quad (6.6)$$

The network model operates by calculating the temperature change for each element (Eq. 6.6) at every time increment, then adding the temperature contribution to the current temperature state. δx and δy are, respectively, the width and height of the elements. The height, δy , is $4.5 \mu\text{m}$ as mentioned earlier. The width, δx , is dependent on the number of elements, n . Specifically, $\delta x = \frac{1}{2} \frac{w}{n}$, where w is

the total width of the membrane, 1100 μm . The model was developed using MATLAB.

The model relies on one key parameter to differentiate fluids— h , the convective heat transfer coefficient between the membrane and the surrounding fluid. The convective heat transfer coefficient is known to be extremely difficult to calculate. Many have studied various methods to calculate the value, from computational methods such as Computational Fluid Dynamics (CFD) [37] to iterative methods [38], but there is no single widely agreed-upon method as of yet. However, it is often related to the Nusselt number—a dimensionless number that captures the convective and conductive heat transfer at a solid-fluid boundary, dependent on the "problem geometry and flow conditions" [39]. A study by Roncati defines the value as $h = \frac{Nu \cdot k}{L}$ [38], where Nu is the Nusselt number, k the thermal conductivity and L the characteristic length. For a given sensor, and thereby a constant length scale, the expression describes a proportional relationship between h and k , the thermal conductivity of the fluid, with Nu being constant for a given solid-fluid boundary. In this project, this proportional relationship is combined with the thermal product heat absorption logic from Equation 5.8 to define a proportional relationship between h and $\sqrt{\rho c_p k}$, the thermal product of the fluid. Despite defining such a relationship, calculating an appropriate magnitude of the convective heat transfer coefficient remains a significant challenge. For the purposes of this project, an initial value of $25 \text{ W m}^{-2} \text{ K}^{-1}$ was taken from Kosky et al. [40] as the upper bound in air under free convection.

6.1.2 Limitations

Limitations of the network model should also be discussed. As mentioned earlier, the model assumes identical convective heat transfer both above and below the membrane. This is not entirely true due to the asymmetric geometry as seen in Figure 6.1. The model also simplifies the convective heat transfer to a single heat transfer coefficient, whereas there are more complex phenomena taking place in actuality. In addition, it is assumed that the membrane is thin enough to collapse the model down to one layer. Whilst this is a relatively good assumption, it is an area for improvement with future updates to the model. Furthermore, the convective heat transfer calculations are performed by assuming a constant external temperature of T_0 . In reality, however, the temperature of the surrounding fluid will vary. Finally, the model only captures heat transfer in two dimensions. Essentially, it assumes an infinite length across the sensor, ignoring lateral conduction. However, the length is actually limited to 1100 μm and lateral conduction is certainly present. Figure 6.4 visualises this phenomenon.

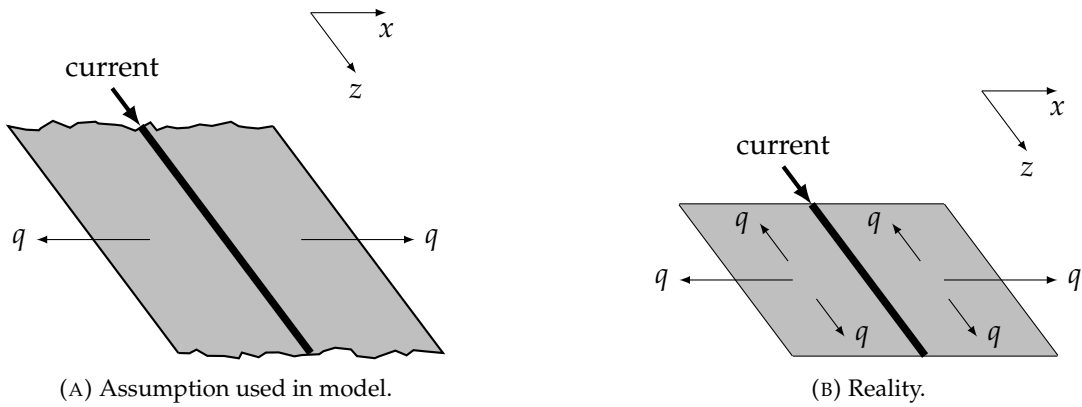


FIGURE 6.4: Network model assumes infinite length of sensor and ignores lateral conduction.

The thermal conductivity, k , is also set as a constant in the model. It is known, however, that the thermal conductivity of a material can vary for several reasons, such as porosity, but particularly temperature and thickness [41]. As Zhu et al. found that "thinner films [of SiO_2] are less sensitive to temperature" [41], the value of thermal conductivity used in this project was $1.4 \text{ W m}^{-1} \text{ K}^{-1}$, the bulk value for SiO_2 published by Touloukian et al. [42]. In the future, this model can be improved by experimentally measuring the thermal conductivity for the particular SiO_2 membrane in the Flusso sensor.

6.2 Experimental Procedure

6.2.1 Soldering Connections

To conduct pulsing experiments with the Flusso sensor, the sensor had to be adapted beyond its conventional use as a gas flow sensor. The sensor is normally operated using a microcontroller through a 10-pin host interface connector. For the purposes of this project, the sensor was used without the microcontroller, but rather soldered for connection to a 9-pin D-sub connector (*Fig. 6.5*) to allow for pulsing through a Proxisense control box. The pin and port position on the Flusso sensor are as shown in Figure 6.6. It is important to note the connections of the two resistors. The first resistor, conventionally used for flow rate measurements, is connected across pins 2 and 5. The second resistor, conventionally used for flow temperature measurements, is connected across pins 3 and 4. Pins 1 and 6 are also internally connected to the flow rate resistor between pins 2 and 5 using a separate set of sensing wires (*Fig. 6.1*). Whilst only the middle resistor was used for the thin-film pulsing experiments, all pins were soldered to allow for flexibility in future experiments. More specifically, the flow rate resistor (pins 2 & 5) was connected to channel 2 and the flow temperature

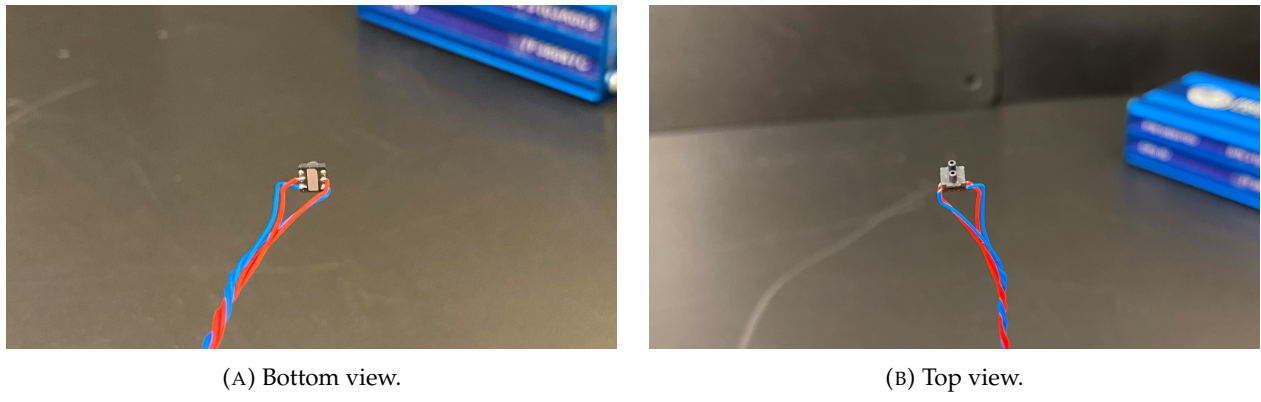


FIGURE 6.5: Flusso MEMS sensor with soldered connections to a 9-pin D-sub connector.

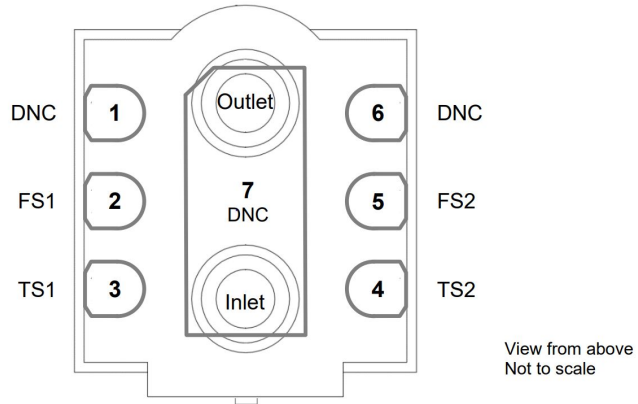


FIGURE 6.6: Pin and port positions on the Flusso sensor. Extracted from Figure 8 of the FLS110 Miniature Gas Flow Sensor Datasheet [36].

resistor (pins 3 & 4) was connected to channel 1 of the 9-pin D-sub connector. This was to maintain consistency with the connections of the Proxisense thin-film channels.

6.2.2 Settings and Procedures

As with the Proxisense sensor in Chapter 5, experimental procedures with the Flusso sensor were consistent with those described in Chapter 4, although the settings were different. Due to its miniature size, the Flusso sensor is significantly more fragile than the Proxisense sensor and physical limits of the sensor must be followed strictly. The absolute maximum ratings for parameters relative to this project are listed in Table 6.1. In particular, the voltage and power limits must be observed with extra caution. As such, initial settings were extremely conservative to ensure the sensor would not be damaged—considering the $128.7\ \Omega$ resistance, the current was set to 10 mA to aim for a safe power input of 12.9 mW. A voltage of 2.0 V was aimed to stay well below the limit of 3.6 V. During execution of

Parameter	Min	Max	Units	Notes
Ambient temperature	-40	+85	°C	
Flow temperature	-40	+85	°C	
Mass flow rate	-2000	+2000	sccm	Through-flow, from inlet port to outlet port
Differential pressure	-5000	+5000	Pa	Inlet port pressure minus outlet port pressure
Flow pressure	200		kPa	Above ambient pressure
Voltage between pins	3.6		V	Between any two functional pins
Flow sensor power	50		mW	

TABLE 6.1: Absolute maximum ratings of the Flusso MEMS sensor for relevant parameters. Adapted from Table 2 of the FLS110 Miniature Gas Flow Sensor Datasheet [36].

the experiment, the current setting was further halved to 5 mA for caution and short pulses of 5 ms were run.

6.3 Preliminary Investigations

The first set of experiments were conducted in air under ambient conditions. Upon running some pulses at 5 mA, it was deemed safe to increase the current up to 10 mA. However, as seen in Figure 6.7, the data would plateau at 5 V. Whilst different parameters were adjusted to single out potential causes of this phenomenon, it was unsuccessful and the decision was made to try pulsing the sensor through a different control box—this solved the plateauing issue. Upon consultation with the developers at Proxisense, it was later realised that different versions of the control box operate in slightly different manners. More specifically, the newer versions, which were initially being used, stepped up the voltage by 5 times. However, the user interface graph was only set to plot up to 5 V and thereby returned results as if the data was plateauing at 5 V. Once switching to an older version of the Proxisense control box, this issue was eliminated.

This problem also meant that the sensor was overpowered significantly. The maximum voltage rating is 3.6 V, as shown in Table 6.1, and the sensor was being pulsed at well over 5 V. As a result, the sensor was being damaged every time the new Proxisense control box was used. Interestingly, its resistance was decreasing with each run. Quantitatively, the sensor's resistance fell from 128.7 Ω to 100.0 Ω in approximately 6 Ω increments over the course of several weeks. Initially, the decreasing resistance could not be explained, as any damage to a resistor typically results in a resistance increase rather than a drop. It is believed, however, that this is the result of an annealing process, similar to that mentioned in Chapter 2. Again, this finding was only later revealed after consulting with the developers at Flusso. Nonetheless, the results with the damaged sensor show some useful preliminary data.

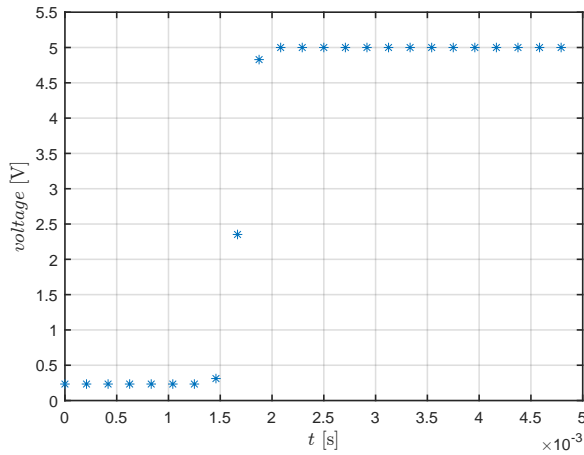


FIGURE 6.7: Pulses with the Flusso sensor at 10 mA would initially completely plateau at 5 V.

6.4 Initial Tests

Once the control box was changed, pulsing experiments returned heat curves without plateauing. Figure 6.8 shows the results, in both a linear scale as well as a \sqrt{t} scale. The data collection and processing, such as the identification of the starting point, were identical to the procedures explained in Chapters 4 & 5. Notice that the plot follows a square root shape extremely well. Whilst this was expected, since the Flusso MEMS sensor fundamentally operates on the same thin-film principle as the Proxisense thin-film gauge, the degree to which the results align was surprising. Also note the lack of starting processes, which were more prominent with the Proxisense sensor, likely due to the Flusso sensor's miniature size allowing for almost instant startup processes. A model could not be fit to these results since an accurate measurement of the sensor's resistance had not been obtained. As mentioned earlier, the sensor's resistance had been dropping and it took several weeks for the phenomenon to be pinpointed and quantified.

With the 10 mA pulses, the voltage stayed below 1.5 V. Therefore, it was determined that it would be safe to raise the current to 15 mA. Figure 6.9 shows the heat curve from the 15 mA pulses. Overall, the data maintains a strong square root curve, with temperature changes close to three times that of the 10 mA pulses (Fig. 6.8). The highest voltage reached by the heat curve is 2.67 V, which equates to 40.0 mW under a current of 15 mA. This is sufficiently high, but still below the maximum rating of 50 mW. As such, a benchmark of approximately 15 mA was used for the current setting.

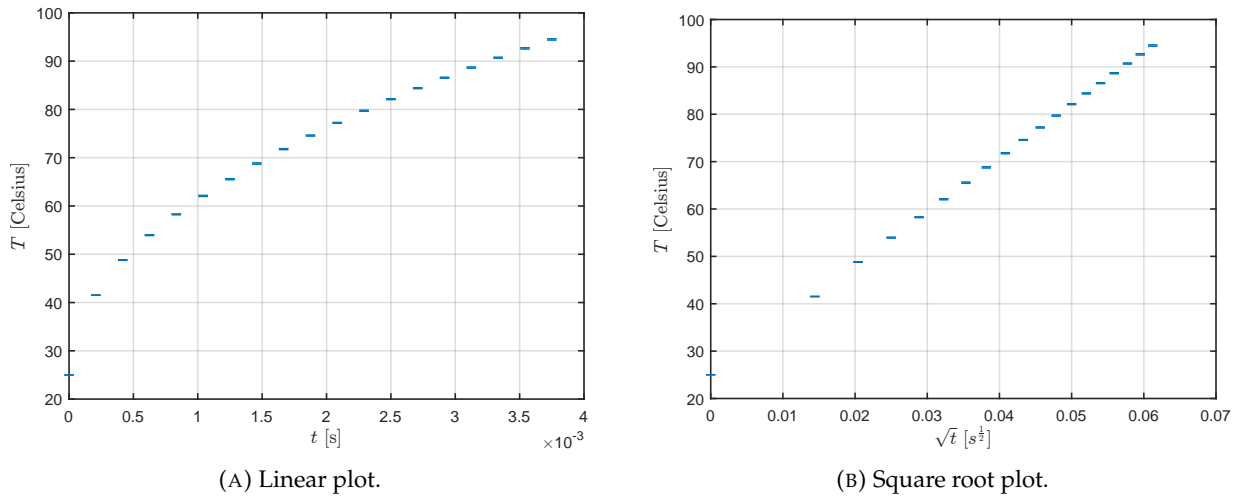


FIGURE 6.8: Pulsing of the Flusso sensor at 10 mA for pulse lengths of 5 ms. Error bars for all plots in Section 6 were placed at one standard deviation from the data point.

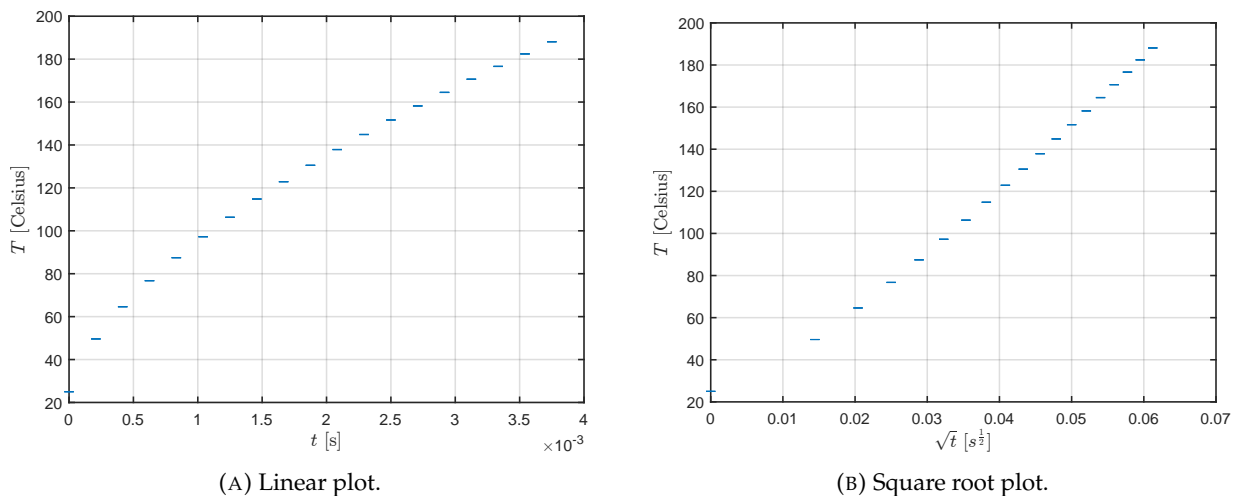


FIGURE 6.9: Pulsing of the Flusso sensor at 15 mA for pulse lengths of 5 ms.

6.5 Preliminary Results: Ambient Air and Flowing Breath

The initial experiments at 10 mA and 15 mA served to check proper operation of the Flusso sensor during pulsing, as the sensor is not conventionally designed for such use. It was also significant to see the square root behaviour of the sensor to confirm thin-film principles. Having gained basic understanding of the Flusso sensor, the next step was to test its ability to differentiate between different gases. The first test conducted was between air and breath. For logistical and safety reasons, these were the easiest gases to test to obtain quick initial data on the Flusso sensor's potential as a gas analyser. Air in the atmosphere contains 78 % nitrogen and 21 % oxygen by volume, along with minimal amounts of other gases such as argon and CO₂ [43]. In comparison, exhaled human breath contains 79 % nitrogen, 13.6-16.0 % oxygen, 4.0-5.3 % CO₂, as well as minimal amounts of other gases and 5.0-6.3 % water vapour [44].

6.5.1 Setup

A plastic tube was connected to the inlet port for the user to exhale into the sensor. Experiments were conducted by starting in ambient air conditions, then flowing breath through the system halfway through the experiment at the 6th pulse (out of 10). Such methods ensure the experiment starts under controlled conditions, highlighting the difference when changes are made to the system.

6.5.2 Results

Figure 6.10 shows the comparison between ambient air and flowing breath. At first glance, it is clear that there is a significant difference between the two gases. Quantitatively, the final temperature for air is 188.077 °C and the final temperature for breath is 165.598 °C. This equates to a percentage difference of 14.8 % which is substantially greater than the differences found with the 1D model for the Proxisense sensor in Chapter 5. Surprisingly, with the implementation of the integral method, the difference falls to 10.3 %. Either way, these differences are significant enough to differentiate the gases beyond signal noise.

However, it should be highlighted that this experiment between air and breath was preliminary for several reasons. First, the thermal properties of breath are highly varying as each run is conducted with newly exhaled breath that is inevitably different to the previous exhalation. Each exhalation can vary across numerous factors, including, but not limited to, temperature, humidity, density, flow rate and gas composition. These inconsistencies are reflected in Figure 6.10, where the data points for

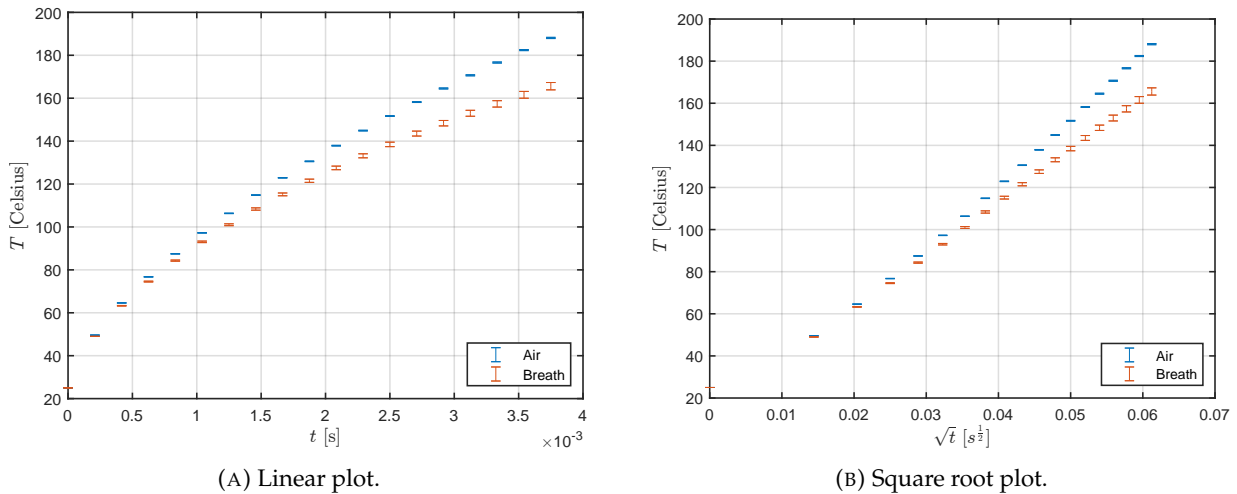


FIGURE 6.10: Result comparison of Flusso sensor pulsing experiments at 15 mA for pulse lengths of 5 ms in air and breath.

breath have significantly larger error bars than those of air. Second, whilst the difference in gas composition between inhaled to exhaled air is known, it is difficult to quantify other contributions such as changes in temperature, humidity and density. In particular, humidity change has a significant effect due to water's high thermal product. Finally, the ambient state of air is inherently different to the flowing state of breath. Despite the low flow rate, it will inevitably influence the nature of the heat transfer occurring within the sensor.

6.6 Preliminary Results: Flowing Air and Flowing Argon

6.6.1 Setup

Having briefly explored the Flusso sensor's capability to differentiate gas composition, a more robust and controlled experiment was set up to compare its performance in air and argon. Since argon was flowed into the system from a high pressure gas cylinder, air was also flowed from a compressor into the system at the same pressure to ensure consistency in flow rate. Specifically, both gases were flowed into the system at 100 kPa gauge pressure and 20 °C fluid temperature. Pressure parameters were set to stay below the absolute maximum ratings displayed in Table 6.1. In particular, a long tube was connected to the outlet port to ensure differential pressure relative to the inlet port remained within limits.

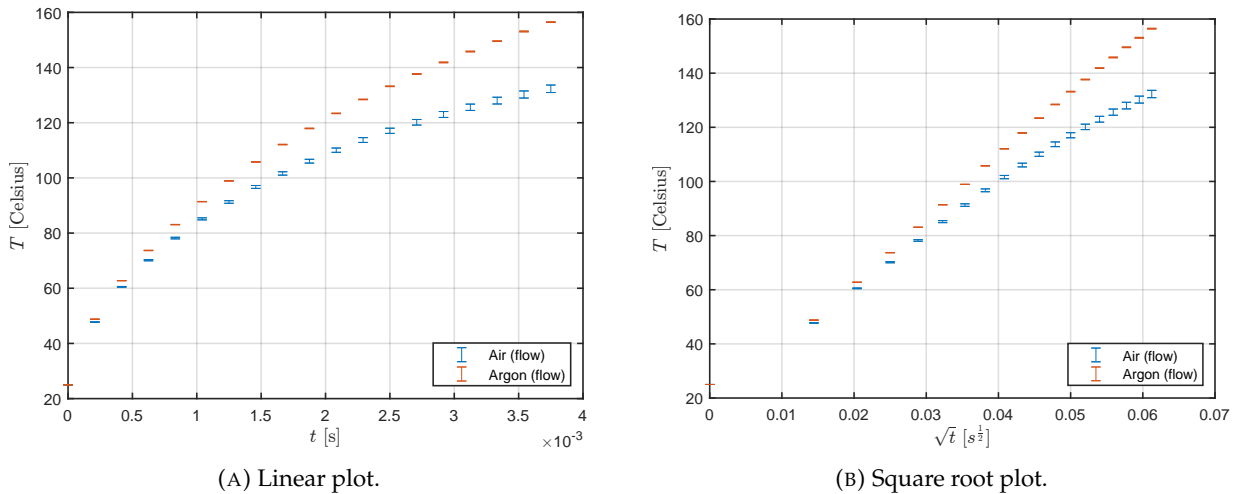


FIGURE 6.11: Result comparison of Flusso sensor pulsing experiments at 15 mA for pulse lengths of 5 ms in flowing air and argon.

6.6.2 Results

The results are as shown in Figure 6.11, where it is possible to see a clear difference between the two gases. Pulses with argon reached 156.449°C , whereas pulses with air reached 132.303°C , equating to a 24.1 K difference. This is a percentage difference of 20.2 %, as well as a 14.9 % difference with the area integral method. Similar to the air-breath experiments, these differences are large enough to differentiate from signal noise. Furthermore, argon's higher final temperature is consistent with the thin-film principle that argon would absorb less thermal energy and result in a higher temperature due to its smaller thermal product. As mentioned in Chapter 1, argon has a thermal product of 3.8676, which is 31.3 % smaller than air's thermal product of 5.6295.

6.7 Undamaged Sensor Results: Ambient Air vs. Argon

6.7.1 Setup

Whilst the results were promising, the air-argon experiments were conducted with a finite fluid velocity through the sensor. Since the Flusso sensor is sensitive to flow by nature, it is critical to conduct experiments in ambient conditions to test its full capability as a gas analyser. Practically, this posed a challenge as argon was only available from a high pressure gas cylinder. Several ideas were raised to overcome this challenge. The first was to build a reservoir system between the cylinder and the sensor. Another idea was to create a sealed container to encapsulate the entire setup. The third option was to purge the system, equalise to atmospheric pressure and shut off the system using a

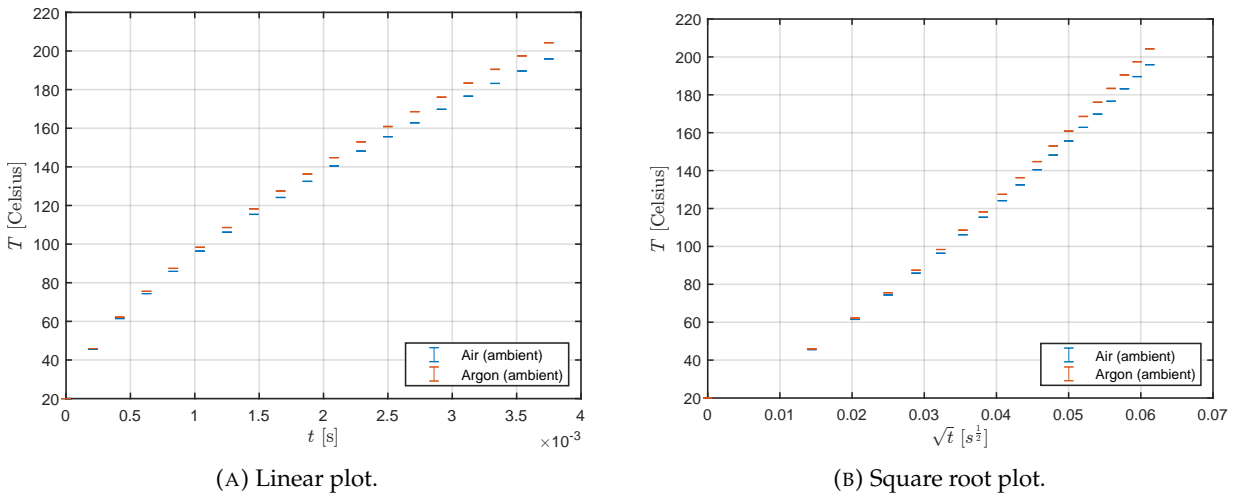


FIGURE 6.12: Result comparison of Flusso sensor pulsing experiments at 15 mA for pulse lengths of 5 ms in ambient air and argon.

valve. Another similar solution using one way valves was also proposed. For logistical reasons, all of these ideas were deemed impractical for the timescale available. The system was instead purged with the test gas, equalised then shut off by manually compressing the tubes rather than using valves.

In addition, it was at this point during the project that the exact cause of the Flusso sensor's resistance decrease had been identified. After several weeks of testing, singling out variables and discussions with Flusso and Proxisense developers, it was realised that occasional use of a newer version of the Proxisense control box had been overpowering and possibly annealing the MEMS sensor. Therefore, from this experiment onward, a new Flusso sensor, with its original resistance of $128.7\ \Omega$, was soldered and set up with a 9-pin D-sub connector.

6.7.2 Results

The results for the ambient experiments between air and argon are presented in Figure 6.12. Whilst the difference is not as large as the previous experiment with flow, it is still noticeable. Quantitatively, air and argon had final temperatures of $195.9023\ ^\circ\text{C}$ and $204.2901\ ^\circ\text{C}$, respectively, amounting to an $8.39\ \text{K}$ (4.66 %) difference. The area integral method returns a percentage difference of 3.62 %. With respective uncertainties of 0.0291 % and 0.0539 % at the end of the pulse for air and argon, the temperature difference is substantial enough to detect beyond noise.

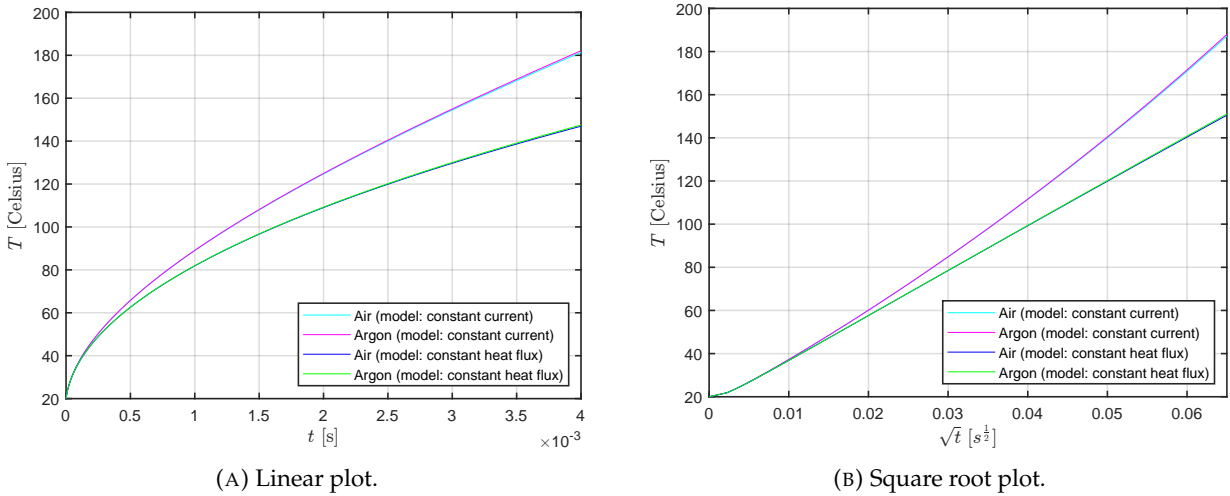


FIGURE 6.13: Original, untuned network model plotted with the initial constant heat flux setting against the updated constant current setting. The network model was executed in $5\ \mu\text{s}$ time increments with 120 discretisations along half the sensor length. Note that there are two pairs of separate model curves that are overlapping.

6.8 Network Model Validation

As these experiments were conducted with a brand new, undamaged Flusso sensor of known thin-film resistance, $128.7\ \Omega$, it is possible to fit the network model to the obtained data. Recall that the model sets an initial value of $25\ \text{W m}^{-2}\ \text{K}^{-1}$ to the convective heat transfer coefficient, h .

With initial parameters set, the generated model clearly overestimates the temperature and only continues to deviate from experimental data as time passes. Furthermore, the difference between air and argon in the model is almost negligible and significantly less than reflected in test data. It was clear that the network model was failing to capture significant aspects of the Flusso sensor's heat transfer. Upon reflection, a major flaw was discovered where initial predictions assumed constant heat flux rather than constant current.

Figure 6.13 shows the initial model predictions of constant heat flux plotted against updated predictions of constant current. With the initial predictions, the heat transfer is captured well in early times but underestimates the temperature in later times. The constant current update considers the rising thin-film resistance and improves the model's predictions at later times.

6.9 Tuned Network Model

Despite changes made to amend such flaws, the model still required the tuning of parameters to match the experimental results. The adjustments were as follows: convective heat transfer coefficient

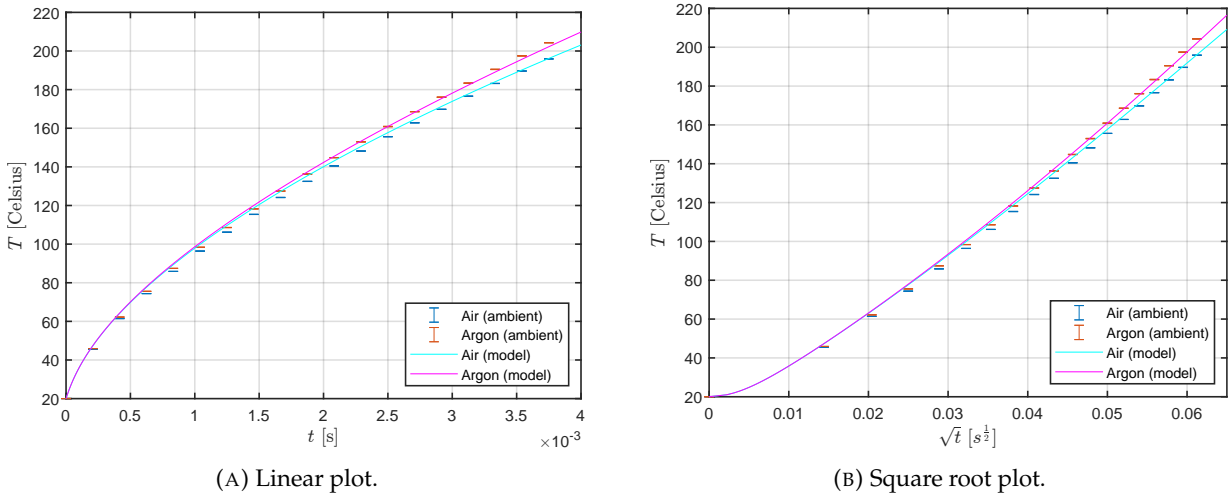


FIGURE 6.14: Flusso sensor pulsing experiments at 15 mA for pulse lengths of 5 ms in ambient air and argon, plotted against the tuned network model. The tuned network model was executed in 5 μ s time increments with 120 discretisations along half the sensor length.

from 25 to 350 $\text{W m}^{-2} \text{K}^{-1}$, membrane thickness from 4.5 to 4.2 μm , membrane density from 2400 to 2700 kg m^{-3} , membrane thermal conductivity from 1.400 to 0.525 $\text{W m}^{-1} \text{K}^{-1}$ and membrane specific heat capacity from 700 to 1200 $\text{J kg}^{-1} \text{K}^{-1}$.

Whilst extensive studies must be conducted on the material properties and internal heat transfer of the Flusso sensor to justify these modifications in a robust manner, it was ensured that each modification was within reasonable range. The adjustment for the convective heat transfer coefficient enlarged the effect of a test gas' thermal product on its heat curve, and accounts for the inclusion of complex convection phenomena, such as buoyancy, present due to the microscale nature of the MEMS sensor. Recall that the coefficient can be defined as $h = \frac{Nu \cdot k}{L}$ [38]—the significant increase from its original value of 25 $\text{W m}^{-2} \text{K}^{-1}$ may also be attributed to the miniature length scale of the sensor. The membrane thickness modification is also within range of possible discrepancies during manufacturing. As for adjustments to the membrane density, thermal conductivity and specific heat capacity, these are consistent with large uncertainties in the material properties of silicon dioxide as mentioned earlier. Such properties can all vary depending on numerous factors but notably crystal structure, manufacturing processes, thickness and temperature. Empirical measurements of each property is necessary to obtain values unique to the Flusso sensor. The tuned network model is presented in Figure 6.14 and aligns significantly better with experimental data.

7 Conclusions & Future Work

In this project, we investigated the research question of how thin-film and MEMS technologies could be exploited to measure gas composition at high frequencies. Using the Flusso MEMS sensor, we were able to significantly improve on current gas analysis technologies, particularly in terms of measurement frequency. However, we have also identified future action items to further develop this technology to reach standards necessary for turbomachinery applications.

7.1 Conclusions

On the current market, the fastest methods of gas sensing require several seconds to obtain data, whereas frequencies of up to 100 kHz would be useful to understand unsteady phenomena in turbomachinery.

To address this deficiency, a novel approach to gas sensing is introduced, utilising the principle of thermal products as a method of identifying unique materials. Specifically, by quantifying thermal products at a sufficiently high SNR, it is possible to identify individual gases, or the composition of a mixture of gases. By pulsing a thin-film, which in itself is essentially a resistor, with a step current, heat is generated and the heat transfer between the film and its surroundings can be quantified. This heat transfer is dependent on the thermal product of the surrounding, which varies with gas concentration. Therefore, the response of the thin-film can be used to measure gas concentration.

To better understand this concept, the Proxisense thin-film gauge was studied. A 1D model, based on a semi-infinite assumption, was introduced to capture the heat transfer at the surface of the thin-film, revealing a proportional relationship between temperature difference and the square root of time. The gradient involved dependency on the thermal products of both the base and the fluid. Alternative modelling techniques were discussed but the simplistic nature of the Proxisense thin-film gauge meant the 1D model was sufficient. Experiments were conducted in water and the data was plotted against the model, which remained accurate until approximately 30 ms. The assumptions in the 1D model, such as zero lateral conduction and zero fluid convection, were no longer true beyond that point. The validated model was used to simulate heat curves of air and argon for pulses

of 30 ms, leading to a conclusion that the Proxisense sensor lacked the sensitivity to differentiate between gases.

The focus shifted to MEMS technology as an approach to further develop the thin-film concept for gas sensing. A MEMS device's miniature size allows for increased frequency and sensitivity. The Flusso FLS110 miniature gas flow sensor was studied as its two tungsten resistors could be treated as thin-films on a fundamental level. Due to key differences in size, structure and material, the 1D model could not be applied and a finite-elements approach was proposed. A network model was developed to discretise the sensor and reproduce the rapid conduction and convection occurring at each element. Whilst the network model was a significant improvement to the 1D model, it remains a challenge to predict the correct response *a priori*.

The concept has been demonstrated experimentally, with the sensor showing good sensitivity to air, argon and exhaled breath. Ambient experiments between air and argon resulted in a 8.39 K difference in final temperatures, equivalent to a 4.66 % difference during the step. This difference is around 100 times larger than the maximum uncertainty of 0.0539 %.

Finally, it is noted that the Flusso sensor ran pulse lengths of 5 ms, equating to a measurement frequency of 200 Hz. As discussed in Chapter 2, the fastest gas analysers on the current market operate at 0.1 Hz, meaning the measurement frequency was increased by three orders of magnitude in this project.

7.2 Future Work

There is significant scope to develop the concept and better understand the behaviour.

First, it would be beneficial to test the current network model on an additional set of data points. The most logical progression was to experiment with different gases, in particular CO₂, although logistical difficulties with hazardous gases proved challenging. Whilst experiments in vacuum conditions were looked into as an alternative, a setup for such tests could not be constructed within the timeline of this project. In addition to being an opportunity to investigate the model's performance in a drastically different thermal product environment, vacuum tests would still be worthwhile as, on the current market, there exists no technology to measure vacuum pressure at high accuracy and frequency. It may allow for a completely different use of the Flusso MEMS sensor as a high frequency vacuum sensor.

With the current network model, the convective heat transfer coefficient varies proportionally with the thermal product, $\sqrt{\rho c_p k}$, of the fluid. However, this can further be improved using more

sophisticated technology such as ANSYS. By modelling the exact geometry of the Flusso sensor, it is possible to accurately simulate the convective heat transfer within the sensor. It would be significant to investigate complex convective phenomena such as buoyancy that may be present at the miniature length and time scales the Flusso sensor operates with.

In addition, better understanding of the SiO_2 material of the Flusso sensor's membrane would improve on another parameter of the network model in the form of thermal conductivity, k . As mentioned in Chapter 6, the thermal conductivity of the membrane can vary depending on its thickness, temperature and crystalline structure. An investigation into these factors will return critical data for better approximation of the k value.

The network model itself could also be developed from 2D to 3D, capturing more dimensions of heat transfer with greater accuracy. This can realistically be approached in two ways: building on the current model in MATLAB, or setting up a finite-elements or conjugate simulation. Either way, the required computational power and duration will significantly increase. However, to obtain the most accurate model for post-processing curve fitting, it is likely that such a process ultimately becomes necessary.

Beyond the model, there are physical improvements that could be made to the sensor itself. Despite a significant increase in measurement frequency, the 200 Hz achieved in this project is still short of the $\approx 100 \text{ kHz}$ desired in turbomachinery. The frequency can be increased by decreasing the pulse lengths but such a change also lowers sensitivity. There are two approaches to maintaining sensitivity with shorter pulse lengths: a more robust sensor that can withstand higher maximum voltage and power ratings or a physically smaller sensor that experiences a larger temperature rise with the same power settings.

Finally, the physical design can also be adapted for turbomachinery applications. Currently, the Flusso sensor can only operate in two flow modes as shown in Figure 6.2. A more non-intrusive method of gas sampling is desirable for measurements in blade film cooling, where the sensor can be directly embedded into experiments.

The changes above would enable full practical application of the thin-film heat transfer approach to gas sensing in obtaining instantaneous and unsteady turbomachinery measurements.

Bibliography

- [1] X. Li, G. Subbuswamy, and J. Zhou, "Performance of Gas Turbine Film Cooling with Backward Injection," *Energy and Power Engineering*, vol. 05, pp. 132–137, Jan. 2013. DOI: 10.4236/epc.2013.54B025.
- [2] I. Monge-Concepción, M. D. Barringer, R. A. Berdanier, K. A. Thole, and C. Robak, "Use of Multiple Tracer Gases to Quantify Vane Trailing Edge Flow Into Turbine Rim Seals," *Journal of Turbomachinery*, vol. 145, no. 1, Oct. 2022, ISSN: 0889-504X. DOI: 10.1115/1.4055445. [Online]. Available: <https://doi.org/10.1115/1.4055445> (visited on 03/23/2023).
- [3] X. Liu, S. Cheng, H. Liu, S. Hu, D. Zhang, and H. Ning, "A Survey on Gas Sensing Technology," *Sensors (Basel, Switzerland)*, vol. 12, no. 7, pp. 9635–9665, Jul. 2012, ISSN: 1424-8220. DOI: 10.3390/s120709635. [Online]. Available: <https://www.ncbi.nlm.nih.gov/pmc/articles/PMC3444121/> (visited on 03/24/2023).
- [4] Geotech, *CO2 Incubator Analyser | Accurate Incubator Verification Tool*, 2016. [Online]. Available: https://www.gemscientific.co.uk/downloads/1598624012Geotech_-_G100_Datasheet_2016GS.pdf (visited on 03/24/2023).
- [5] D. Company, *Devices For The Determination Of The SF6 Gas Quality*, Oct. 2020. [Online]. Available: https://dilo.com/fileadmin/dilo_us/1._SF6_Gas/1._Products/6._Measuring_Devices/1._Gas_Analyzers/PDFs/Multi_Analyzer_SF6/3-038R-RV2-Multi-Analyzer_DS_Rev_2021.pdf (visited on 03/24/2023).
- [6] J. Hilsenrath, C. W. Beckett, W. S. Benedict, *et al.*, "Tables of Thermal Properties of Gases," en, *Journal of The Electrochemical Society*, vol. 103, no. 5, p. 124C, May 1956, Publisher: IOP Publishing, ISSN: 1945-7111. DOI: 10.1149/1.2430297. [Online]. Available: <https://iopscience.iop.org/article/10.1149/1.2430297/meta> (visited on 03/24/2023).
- [7] J. Ahn, S. Mhetras, and J.-C. Han, "Film-Cooling Effectiveness on a Gas Turbine Blade Tip Using Pressure-Sensitive Paint," *Journal of Heat Transfer*, vol. 127, no. 5, pp. 521–530, May 2005,

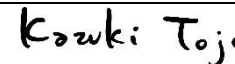
- ISSN: 0022-1481. DOI: 10.1115/1.1909208. [Online]. Available: <https://doi.org/10.1115/1.1909208> (visited on 03/26/2023).
- [8] J. Teloxa, D. Narzary, F. Sierra, J. Lei, F. Carrillo, and J.-C. Han, "Measurement and Modelling of Blade Tip Cooling in Gas Turbines," in *Proceedings of the ASME Turbo Expo*, vol. 3, Jun. 2013. DOI: 10.1115/GT2013-94812. (visited on 03/26/2023).
- [9] K. Clark, M. Barringer, K. Thole, *et al.*, "Using a Tracer Gas to Quantify Sealing Effectiveness for Engine Realistic Rim Seals," en, American Society of Mechanical Engineers Digital Collection, Sep. 2016. DOI: 10.1115/GT2016-58095. [Online]. Available: <https://asmedigitalcollection.asme.org/GT/proceedings-abstract/GT2016/49781/240395> (visited on 03/26/2023).
- [10] R. A. Berdanier, I. Monge-Concepción, B. F. Knisely, M. D. Barringer, K. A. Thole, and E. A. Grover, "Scaling Sealing Effectiveness in a Stator–Rotor Cavity for Differing Blade Spans," *Journal of Turbomachinery*, vol. 141, no. 5, Jan. 2019, ISSN: 0889-504X. DOI: 10.1115/1.4042423. [Online]. Available: <https://doi.org/10.1115/1.4042423> (visited on 03/26/2023).
- [11] R. K. Jha, "Non-Dispersive Infrared Gas Sensing Technology: A Review," *IEEE Sensors Journal*, vol. 22, no. 1, pp. 6–15, Jan. 2022, Conference Name: IEEE Sensors Journal, ISSN: 1558-1748. DOI: 10.1109/JSEN.2021.3130034.
- [12] T. Yasuda, S. Yonemura, and A. Tani, "Comparison of the Characteristics of Small Commercial NDIR CO₂ Sensor Models and Development of a Portable CO₂ Measurement Device," en, *Sensors*, vol. 12, no. 3, pp. 3641–3655, Mar. 2012, Number: 3 Publisher: Molecular Diversity Preservation International, ISSN: 1424-8220. DOI: 10.3390/s120303641. [Online]. Available: <https://www.mdpi.com/1424-8220/12/3/3641> (visited on 03/26/2023).
- [13] S. Sensortech, *Introduction to Electrochemical (EC) Gas Sensors*, Feb. 2007. [Online]. Available: <https://www.sgxsensorstech.com/content/uploads/2014/08/Introduction-to-Electrochemical-EC-Gas-Sensors1.pdf> (visited on 03/26/2023).
- [14] H. Wan, H. Yin, and A. J. Mason, "Rapid measurement of room temperature ionic liquid electrochemical gas sensor using transient double potential amperometry," en, *Sensors and Actuators B: Chemical*, vol. 242, pp. 658–666, Apr. 2017, ISSN: 0925-4005. DOI: 10.1016/j.snb.2016.11.103. [Online]. Available: <https://www.sciencedirect.com/science/article/pii/S0925400516319013> (visited on 03/27/2023).
- [15] R. Cavicchi, *Calorimetric Sensors*, en. Momentum Press, Highland Park, NJ, Apr. 2011. [Online]. Available: https://tsapps.nist.gov/publication/get_pdf.cfm?pub_id=903256.

- [16] H. M. McNair, J. M. Miller, and N. H. Snow, *Basic Gas Chromatography*, en. John Wiley & Sons, Sep. 2019, Google-Books-ID: VimjDwAAQBAJ, ISBN: 978-1-119-45075-7.
- [17] D. L. Schultz and T. Jones, "Heat-transfer measurements in short-duration hypersonic facilities," Advisory Group for Aerospace Research and Development, Tech. Rep. AG-165, Jan. 1973, p. 156. (visited on 03/27/2023).
- [18] M. Collins, K. Chana, and T. Povey, "New technique for the fabrication of miniature thin film heat flux gauges," en, *Measurement Science and Technology*, vol. 26, no. 2, p. 025303, Jan. 2015, Publisher: IOP Publishing, ISSN: 0957-0233. DOI: 10.1088/0957-0233/26/2/025303. [Online]. Available: <https://dx.doi.org/10.1088/0957-0233/26/2/025303> (visited on 03/28/2023).
- [19] J.-F. Lei and H. A. Will, "Thin-film thermocouples and strain-gauge technologies for engine applications," en, *Sensors and Actuators A: Physical*, vol. 65, no. 2, pp. 187–193, Mar. 1998, ISSN: 0924-4247. DOI: 10.1016/S0924-4247(97)01683-X. [Online]. Available: <https://www.sciencedirect.com/science/article/pii/S092442479701683X> (visited on 03/28/2023).
- [20] K. J. Irimpan, N. Mannil, H. Arya, and V. Menezes, "Performance evaluation of coaxial thermocouple against platinum thin film gauge for heat flux measurement in shock tunnel," en, *Measurement*, vol. 61, pp. 291–298, Feb. 2015, ISSN: 0263-2241. DOI: 10.1016/j.measurement.2014.10.056. [Online]. Available: <https://www.sciencedirect.com/science/article/pii/S0263224114005259> (visited on 03/28/2023).
- [21] S. M. Guo, C. C. Lai, T. V. Jones, M. L. G. Oldfield, G. D. Lock, and A. J. Rawlinson, "The application of thin-film technology to measure turbine-vane heat transfer and effectiveness in a film-cooled, engine-simulated environment," en, *International Journal of Heat and Fluid Flow*, vol. 19, no. 6, pp. 594–600, Dec. 1998, ISSN: 0142-727X. DOI: 10.1016/S0142-727X(98)10034-6. [Online]. Available: <https://www.sciencedirect.com/science/article/pii/S0142727X98100346> (visited on 03/28/2023).
- [22] S. M. Guo, M. C. Spencer, G. D. Lock, T. V. Jones, and N. W. Harvey, "The Application of Thin Film Gauges on Flexible Plastic Substrates to the Gas Turbine Situation," en, American Society of Mechanical Engineers Digital Collection, Feb. 2015. DOI: 10.1115/95-GT-357. [Online]. Available: <https://asmedigitalcollection.asme.org/GT/proceedings-abstract/GT1995/78811/246777> (visited on 03/28/2023).

- [23] K. Chana, "Practical on and off-wing Applications of a Thermal Product Measurement Sensor for Detection of Contamination in Fluids," in *MP-AVT-306-20*, NATO STO, Nov. 2018, ISBN: ISBN 978-92-837-2207-6. DOI: 10.14339/STO-MP-AVT-306-20-PDF. (visited on 03/26/2023).
- [24] E. L. W. Gardner, A. De Luca, J. Coull, C. Lee, and F. Udrea, "On the Design of the World's Smallest Flow Sensor Package," *IEEE Sensors Letters*, vol. 5, no. 6, pp. 1–4, Jun. 2021, Conference Name: IEEE Sensors Letters, ISSN: 2475-1472. DOI: 10.1109/LSENS.2021.3077959.
- [25] Proxisense, *Our History*, en-gb. [Online]. Available: <https://www.proxisense.com/our-history-2/> (visited on 03/28/2023).
- [26] Proxisense, *Thermal Product Sensing*, en-gb. [Online]. Available: <https://www.proxisense.com/thermal-product-sensing/> (visited on 03/28/2023).
- [27] F. Ltd., *Home*, en. [Online]. Available: <https://flussoltd.com/> (visited on 03/28/2023).
- [28] F. Ltd., *FLS110 Mass Flow Sensor*, en. [Online]. Available: <https://flussoltd.com/products/fls110-mass-flow-sensor> (visited on 03/28/2023).
- [29] D. C. Giancoli, *Physics: principles with applications*, eng, 4th ed. Englewood Cliffs, N.J: Prentice Hall, 1995, Open Library ID: OL1120034M, ISBN: 978-0-13-102153-2.
- [30] K. A. Morris, "What is Hysteresis?" *Applied Mechanics Reviews*, vol. 64, no. 5, Aug. 2012, ISSN: 0003-6900. DOI: 10.1115/1.4007112. [Online]. Available: <https://doi.org/10.1115/1.4007112> (visited on 03/31/2023).
- [31] J. P. Holman, *Heat Transfer: Tenth Edition*, en. McGraw-Hill Education, 2010, Google-Books-ID: 7TGGPwAACAAJ, ISBN: 978-0-07-352936-3.
- [32] A. Inc., *Ansys | Engineering Simulation Software*, en-GB. [Online]. Available: <https://www.ansys.com/en-gb> (visited on 05/16/2023).
- [33] Y. Nakasone, S. Yoshimoto, and T. A. Stolarski, "Chapter 2 - Overview of ANSYS Structure and Visual Capabilities," en, in *Engineering Analysis with ANSYS Software*, Y. Nakasone, S. Yoshimoto, and T. A. Stolarski, Eds., Oxford: Butterworth-Heinemann, Jan. 2006, pp. 37–50, ISBN: 978-0-7506-6875-0. DOI: 10.1016/B978-0750668750500326. [Online]. Available: <https://www.sciencedirect.com/science/article/pii/B9780750668750500326> (visited on 03/31/2023).
- [34] P. Evans, *Properties of water at atmospheric pressure*, en-GB, Mar. 2015. [Online]. Available: <https://theengineeringmindset.com/properties-of-water-atmospheric-pressure-saturated-liquid/> (visited on 04/03/2023).

- [35] C. I. L. bibinitperiod Materials, "MACOR Machinable Glass Ceramic," en, [Online]. Available: <https://psec.uchicago.edu/ceramics/MACOR%20Data%20Sheet.pdf> (visited on 04/04/2023).
- [36] F. Ltd., *FLS110 Miniature Gas Flow Sensor Datasheet*, May 2022. (visited on 04/07/2023).
- [37] H. B. Awbi, "Calculation of convective heat transfer coefficients of room surfaces for natural convection," en, *Energy and Buildings*, vol. 28, no. 2, pp. 219–227, Oct. 1998, ISSN: 0378-7788. DOI: 10.1016/S0378-7788(98)00022-X. [Online]. Available: <https://www.sciencedirect.com/science/article/pii/S037877889800022X> (visited on 04/12/2023).
- [38] D. Roncati, "Iterative calculation of the heat transfer coefficient," *Progettazione Ottica Roncati, Italy*, 2013.
- [39] M. Malekan, A. Khosravi, and M. El Haj Assad, "Chapter 6 - Parabolic trough solar collectors," en, in *Design and Performance Optimization of Renewable Energy Systems*, M. E. H. Assad and M. A. Rosen, Eds., Academic Press, Jan. 2021, pp. 85–100, ISBN: 978-0-12-821602-6. DOI: 10.1016/B978-0-12-821602-6.00007-9. [Online]. Available: <https://www.sciencedirect.com/science/article/pii/B9780128216026000079> (visited on 04/12/2023).
- [40] P. Kosky, R. Balmer, W. Keat, and G. Wise, "Chapter 14 - Mechanical Engineering," en, in *Exploring Engineering (Fifth Edition)*, P. Kosky, R. Balmer, W. Keat, and G. Wise, Eds., Academic Press, Jan. 2021, pp. 317–340, ISBN: 978-0-12-815073-3. DOI: 10.1016/B978-0-12-815073-3.00014-4. [Online]. Available: <https://www.sciencedirect.com/science/article/pii/B9780128150733000144> (visited on 04/12/2023).
- [41] W. Zhu, G. Zheng, S. Cao, and H. He, "Thermal conductivity of amorphous SiO₂ thin film: A molecular dynamics study," en, *Scientific Reports*, vol. 8, no. 1, p. 10537, Jul. 2018, Number: 1 Publisher: Nature Publishing Group, ISSN: 2045-2322. DOI: 10.1038/s41598-018-28925-6. [Online]. Available: <https://www.nature.com/articles/s41598-018-28925-6> (visited on 04/08/2023).
- [42] Y. S. Touloukian, R. W. Powell, C. Y. Ho, and P. G. Klemens, "Thermophysical Properties of Matter - The TPRC Data Series. Volume 2. Thermal Conductivity - Nonmetallic Solids," en, Thermophysical and Electronic Properties Information Analysis Center Lafayette IN, Data book ADA951936, Jan. 1971, Section: Technical Reports. [Online]. Available: <https://apps.dtic.mil/sti/citations/ADA951936> (visited on 04/08/2023).

- [43] D. R. Williams, *Earth Fact Sheet*, Fact Sheet, Dec. 2021. [Online]. Available: <https://nssdc.gsfc.nasa.gov/planetary/factsheet/earthfact.html> (visited on 04/11/2023).
- [44] P. S. Dhami, G. Chopra, and H. N. Shrivastava, *Pradeep's A Text Book of Biology for Class 12*, English, 2019-2020. Pradeep Publications, 2019, ISBN: 978-81-939192-6-2. (visited on 04/11/2023).

Description of 4YP task or aspect being risk assessed here: <i>(Read the Guidance Notes before completing this form)</i> Reducing Aviation Emissions: Gas Sensing for Cooling and Combustion using Micro-Electro-Mechanical-Systems <p>It is imperative that we minimise the impact of air travel on our environment. To achieve this, we need to (1) drastically increase jet engine efficiency, for example by increasing turbine entry temperatures, and (2) develop new combustors for carbon-neutral synthetic fuel and ultimately Hydrogen.</p> <p>This project will support both efforts by developing a new technique for sensing gas concentration. This will enable us to improve our fundamental understanding of: (1) cooling effectiveness, e.g. by feeding cooling holes with a foreign gas and tracing its dispersion through the flow field, and (2) the development and control of combustion processes.</p> <p>Our new technique will employ miniature Micro-Electrical-Mechanical-Systems (MEMS) devices developed by Flusso Ltd (https://flussoltd.com/). Conventionally these sensors are used to measure mass flow but we will use them in a different operating mode which is sensitive to mass flow of air.</p> <p>The project will focus on modifying an existing sensor designed for mass flow measurements to operate in a pulsed mode to measure thermal product of air. Initially, a model will be created that will be calibrated against distilled water using an existing thermal product system. Subsequently, the Flusso MEMS sensor will be converted for use with the thermal product electronics.</p>		4YP Project Number: 12705
Site, Building & Room Number: Southwell Building, OTRF Storage and Calibration Room (363.10.34)	Other Relevant risk Assessments: N/A	
Assessment undertaken by: Kazuki Tojo	Signed: 	Date: 21/04/2023
Assessment Supervisor: John Coull, Kam Chana	Signed: 	Date: 21/04/2023

Assessing the Risk*		RISK MATRIX		LIKELIHOOD (or probability)			
				High	Medium	Low	Remote
CONSEQUENCES	Severe	High	High	Medium	Low		
	Moderate	High	Medium	Medium/Low	Effectively Zero		
	Insignificant	Medium/Low	Low	Low	Effectively Zero		
	Negligible	Effectively Zero	Effectively Zero	Effectively Zero	Effectively Zero		

You can do this for each hazard as follows:

- Consequences:** Decide how severe the outcome for each hazard would be if something went wrong (i.e. what are the Consequences?) Death would be "Severe", a minor cut to a finger could be regarded as "Insignificant".
- Likelihood:** How likely are these Consequences to actually happen? Highly likely? Remotely likely, or somewhere in between?
- Risk Rating:** Start at the left of the coloured Matrix. On your chosen Consequences row, read across until you are in the correct Likelihood column for the hazard in question. For example, an outcome with Severe consequences but with a Low probability of actually happening equates to a Medium risk overall. In this case "Medium" is what should be written in the Risk.

Overall statement of risk

- Carefully consider the risks associated with your project, the nature of the activity with which you will be engaged, and its location.
- Check the information from Health and Safety pages in the intranet including those specifically for the 4YP.

Students must discuss these risks with their supervisor.

- Office work only.** My project involves only basic office work (paper and computers). It does not involve hands-on laboratory or field work of any kind. I am aware of the associated risks, including the health risks associated with the extended use of computers and display screens. No further assessment is required.
- Low Risk.** I consider the health and safety risks associated with my project to be low, working in alignment with existing risk assessments, I have referenced relevant risk assessments above and have agreed with my supervisor that no further assessment is required. For example, collecting data from existing systems within a lab.
- Medium Risk.** I consider there to be additional risks associated with my project as it requires risk assessment authorisation below:

Risk Assessments for Hazardous Substances & Biological Materials. The Biological & Chemical Safety Officer's (BCSO) signature is required for the final sign-off on Engineering Science COSH Assesments. If the BCSO is unavailable the DSO can provide this signature. For IBME, the IBME Safety Officer can provide this signature. Reference E refers. The BCSO's signature is also required for risk assessments involving the use of biological materials.

Genetically Modified Organisms. Risk assessments involving genetically modified organisms require the BSCO's signature as well as approval from the Genetic Modification Safety Committee for the work to proceed. The department's Safety Policy refers.

Laser Risk Assessments: In addition to the supervisor of the laser equipment/experiment concerned, the Department Laser Safety Officer (DLSO) must also sign risk assessments involving lasers.

Where Specialist Safety Officers Originate Risk Assessments. Where the DSO or Specialist Safety Officers write, co-write or otherwise originate risk assessments they will be required to sign and authorize such risk assessments.

Requirements for review by specialists should be identified within Safety Requirements section on <https://fouryp.eng.ox.ac.uk/resourcetimepreview2.php>

- High Risk.** This is a high risk activity as identified by Specialist Safety Officers.

Please review with Specialist Safety Officers where projects are Medium Risk sign below, ask your supervisor to countersign and then submit to Sharepoint site.

Signature of student:	Signature of supervisor:
Date: <i>Kawki Tojo</i>	<i>JK Schana</i> Date: 21/04/2023

Hazard (<i>potential for harm</i>)	Persons at Risk	Risk Controls In Place (<i>existing safety precautions</i>)	Risk*	Future Actions identified to Reduce Risks (<i>but not in place yet</i>)
Sensor powered by USB from laptop	User of sensor	Make sure hands are dry when inserting USB	Effectively zero	N/A
Posture issues, sore eyes from use of computer display	User of computer	Sit with correct posture Rest eyes when they get tired 5/10 min breaks every hour	Effectively zero	N/A
Glass beaker breaking	User of beaker	Handle with caution with both hands Use gloves if breakage occurs	Low	N/A
Use of isopropanol (very small amounts) for cleaning of sensor	User of isopropanol	Use gloves Only use necessary amounts of fluid (very small amounts for cleaning)	Low	N/A
Possibility of road accident enroute to building	Researcher	Wear reflective gear Wear helmet Ride bike with caution, aware of surrounding	Medium	N/A
Gas cylinder accidents	User of gas cylinder	Only operated by qualified technician Student (Kazuki Tojo) does not operate cylinder in any way	Low	N/A
Electricity accidents when using water bath	User of water bath	Always dry hand before touching electronics, electronics is low power	Effectively zero	N/A